Article

Cell nucleus as a microrheological probe to study the rheology of the cytoskeleton

Moslem Moradi[1] and Ehssan Nazockdast[1,*]
[1]UNC Chapel Hill, Applied Physical Sciences, Chapel Hill, North Carolina

ABSTRACT   Mechanical properties of the cell are important biomarkers for probing its architectural changes caused by cellular processes and/or pathologies. The development of microfluidic technologies has enabled measuring the cell's mechanical properties at high throughput so that mechanical phenotyping can be applied to large samples in reasonable timescales. These studies typically measure the stiffness of the cell as the only mechanical biomarker and do not disentangle the rheological contributions of different structural components of the cell, including the cell cortex, the interior cytoplasm and its immersed cytoskeletal structures, and the nucleus. Recent advancements in high-speed fluorescent imaging have enabled probing the deformations of the cell cortex while also tracking different intracellular components in rates applicable to microfluidic platforms. We present a, to our knowledge, novel method to decouple the mechanics of the cell cortex and the cytoplasm by analyzing the correlation between the cortical deformations that are induced by external microfluidic flows and the nucleus displacements, induced by those cortical deformations, i.e., we use the nucleus as a high-throughput microrheological probe to study the rheology of the cytoplasm, independent of the cell cortex mechanics. To demonstrate the applicability of this method, we consider a proof-of-concept model consisting of a rigid spherical nucleus centered in a spherical cell. We obtain analytical expressions for the time-dependent nucleus velocity as a function of the cell deformations when the interior cytoplasm is modeled as a viscous, viscoelastic, porous, and poroelastic material and demonstrate how the nucleus velocity can be used to characterize the linear rheology of the cytoplasm over a wide range of forces and timescales/frequencies.

SIGNIFICANCE   Deforming cells in microchannels using fluidic forces yields high-throughput rates, making this tool suitable for diagnosing and separating diseased cells in clinical applications. However, measurements using this technique thus far have not considered the composite nature of the structure and mechanics of the cell. Meanwhile, recent advancements in microfluidics and high-speed imaging allow us to probe the deformations of the cellular boundaries while also tracking the movements of intracellular components. Motivated by these advancements, this work proposes a theoretical framework that uses the measured displacements of the cellular boundary and the nucleus to calculate the time-dependent mechanics of the cytoplasm, independently of the cortex mechanics.

INTRODUCTION

Extensive research over the past few decades has demonstrated the key role of the cell's mechanical aspects in many cellular processes (1), including mechanotransduction (2), cell motility (2), division (3,4), and differentiation (5). The ability of the cell to generate and respond to forces is controlled by its cytoskeleton: a highly dynamic and heterogeneous assembly of biopolymers, cross-linkers, and motor proteins (6). Moreover, many malignancies involve large variations in the cytoskeletal and nuclear organizations,

which naturally lead to variations in cell mechanics. Thus, cell mechanics provides a label-free biomarker for determining cell types, the cell cycle stage, division rate, and disease state, among other things (7,8).

The main structural components that determine the mechanics of eukaryotic cells are 1) the cell membrane and the cortical network of actin filaments attached to it (referred to as the cell cortex hereafter), 2) the cell nucleus composed of the nuclear membrane and the nucleoplasm within, and 3) the cell cytoplasm that fills the volume between the cell cortex and the nucleus, as well as the cytoskeletal assemblies within the cytoplasm. These include the microtubule asters bound to the nuclear membrane and the immersed intermediate filament networks. In this work, we refer to the cytoplasm and its embedded structures

---

as simply cytoplasm and refer to the cytoplasmic fluid as cytosol.

The cell's mechanical response to external forces and boundaries is determined by force transport within each of these structures and across their interfaces. Indeed, a large number of careful experiments suggest that the cell cortex and the cytoplasm have two distinct time-dependent mechanical behaviors (9,10) and that the cell nucleus is the stiffest component between these three structures (11). We also know that different malignancies and cellular processes may have different effects on these three components. For example, taxol is a drug used in cancer therapy that acts through the disruption of microtubule assembly and cell division within the cytoplasm (12). On the other hand, the softness of cancerous cells is associated with the disruption of the cortical actin network (13), whereas many diseases involve changes in nuclear architecture and shape (8). Thus, to explore these structural changes, it is essential to have a measure of the relative contribution of each of these structures to the overall mechanical response in the experimental techniques.

The probe-based (local) techniques—including atomic force microscopy (14), passive particle-tracking microrheology, active microrheology using optical tweezers, and magnetic particles (15)—have the advantage of exploring the local (cell cortex, cytoplasm, and the nucleus) mechanical response over a wide range of forces and frequencies (timescales). These methods are, however, low throughput (less than 100 cell per hour). Cells of different type, size, cell cycle stage, and malignancies can have significantly different cytoskeletal and nuclear organizations and mechanical properties. This makes applying these methods to large and heterogeneous population of cells very challenging.

In contrast, serial deformations of cells in microfluidic platform through hydrodynamic forces enables throughput rates of 100–1000 cells per second, which makes them suitable for clinical applications. Gossett et al. combined high-speed imaging with cell deformation in extensional flows and used the ratio of the longest (stretched)/shortest (compressed) axes of the cells as a measure of cell deformability to separate diseased and healthy cells (16). Mietke et al. used the analytical solution of the flow around a spherical cell in an axisymmetric cylindrical channel to compute the fluid stresses on the cell and compute the steady-state deformation of the cell, assuming small deformations and modeling the cell as an elastic shell or sphere (17). The predicted shapes were compared against the cell shapes from microscopy to extract the elastic properties of the cell in both bulk and shell models. Mokbel et al. used numerical simulations to extend these calculations to finite deformations, in which they modeled the cell as a viscoelastic material surrounded by a thin elastic shell (18). Most recently, Fregin et al. used dynamic real-time deformability cytometry to simultaneously measure the apparent elastic and viscous properties of a cell without solving for the detailed fluid flows and deformation fields (19).

One limitation of these studies is that they do not explicitly account for the nucleus in their mechanical models. However, we know that the nucleus/whole-cell size ratio, which is a purely geometrical factor, can largely change the apparent stiffness and fluidity of the cell (20,21).

Another limitation of these studies is that they have not explored the time-dependent mechanics of the cytoplasm (17,19). However, previous microrheological measurements show that the elastic and viscous responses of the cytoplasm and its immersed cytoskeleton are generally time dependent (22,23). Because of the highly dynamic and hierarchical structures immersed in cytoplasm, its rheology can vary significantly with the time- and length scale of the measurements (24–29). This complexity in structure and mechanical response has also led to several competing theories for describing the rheology of the cytoplasm. In the continuum limit, the cytoplasm has been modeled as a viscoelastic material, a porous gel, an active gel, and a soft glassy material (30–35).

Recent technologies in fluorescent and high-speed imaging have enabled simultaneous tracking of the time-dependent shape of the cell cortex and displacements of different intracellular components, particularly the nucleus, with high spatial and temporal resolution as the cells flow through the microchannels (36–38). These advancements offer the opportunity to build upon the previous theories and experiments and devise techniques for high-throughput time-dependent mechanical characterization of different cellular components. Yet the modeling framework for deploying these rich data is underdeveloped.

The aim of this study is to use the time-dependent deformation of the cell cortex and the displacement of the cell nucleus to determine the time-dependent mechanics of the cytoplasm independent of the cortex mechanics. Specifically, we use the nucleus as a microrheological probe to study the cytoplasm mechanics. Unlike the typical microrheology experiments in which the probe's motion is driven by thermal forces (passive microrheology) or external forces (active microrheology), in our system the motion of the nucleus is driven by the deformations of the cell boundary (cortex), which itself is induced by external microfluidic flows.

Given that the nucleus is significantly stiffer than the cell cortex, in the first step we model the nucleus as a rigid sphere. Assuming the cortex deformations are known through experiment, the nucleus velocity is entirely determined by the rheology of the cytoplasm and the size of the nucleus, irrespective of the mechanics of the cortex. To make analytical progress, we consider a proof-of-concept model consisting of a spherical nucleus centered in a spherical cell and provide analytical solutions to the cytoplasm velocity field and the nucleus velocity as a function of the rate of displacement of the cortex at small

deformations. We model the cytoplasm as viscous, porous, viscoelastic, and poroelastic media and explore the effect of the constitutive parameters, such as relaxation time in the Maxwell equation and permeability and network relaxation time in poroelastic models, in the time-dependent relationships between cell cortex surface velocity modes and the ensuing nucleus velocity.

The choice of the appropriate constitutive equation (CE) is determined by microstructural parameters of the cytoskeleton, including the composition of different filaments and their cross-linking dynamics (39–42). Uncovering these relationships generally requires a combination of mesoscopic simulations and theories of nonequilibrium statistical mechanics, which is outside of the scope of this study. Rather, our goal is to determine the coefficients that appear in the existing classes of CEs by combining continuum modeling with the cellular deformation data from microfluidic channels.

METHODS

Cell deformations under external flows are determined by the balance between the forces exerted on the cortex from the outer fluid, $\mathbf{f}_O$; forces induced by the interior cytoplasm, $\mathbf{f}_I$; and the forces induced by the cortex deformations, $\mathbf{f}_M$. In the absence of inertial forces in the Stokes regime, the sum of these forces is identically zero: $\mathbf{f}_O + \mathbf{f}_I + \mathbf{f}_M = 0$. Assuming we can track the cell surface, one can compute the outer fluid flow and its associated forces by solving the Stokes flow and imposing a no-slip boundary condition (BC) on the cell's outer surface; see Fig. 1 b. In the presence of a constitutive model for the cortex, $\mathbf{f}_M$ can be computed as a function of its time-dependent displacements. Hence, we can compute $\mathbf{f}_I = -(\mathbf{f}_O + \mathbf{f}_M)$, which can be used to extract the coefficients of the presumed form of the CE for the cell cytoplasm. In other words, determining the rheology of the interior cytoskeleton requires specifying the CE for the cortex.

Here, we propose an alternative route that allows determining the rheology of the cytoplasm independent of the cortex mechanics. The main assumption here is that the cell's surface and the nucleus velocities are known through experiments. We use this surface velocity as a BC, whereas the BCs for the nucleus are no slip and zero net force. This provides sufficient conditions for computing the internal cytoplasmic flows when complemented with the

appropriate form of momentum equation for viscous, viscoelastic, porous, and poroelastic materials. Note that these calculations are completely decoupled from the cortex mechanics. The remaining assumptions, enumerated below, are made for simplicity and to allow analytical progress. The methodology presented here can still be applied even when these assumptions are relaxed, but the equations of motion may need to be solved numerically. These assumptions are 1) the nucleus is modeled as a rigid sphere, 2) the nucleus is centered in a spherical cell, and 3) the deformations of the cell boundary and the net displacement of the nucleus are assumed to be small so that the geometry remains concentric. In these conditions, the flow within the cytoplasm is axisymmetric in spherical coordinates.

In the next sections, we present our analytical results of the nucleus velocity as a function of the rates of deformations of the cell cortex, when the cytoplasm is a Newtonian fluid, a viscoelastic fluid, a porous material, and a poroelastic network. To facilitate the use of these analytical expressions and for further clarity, we reproduce the detailed steps taken to obtain the final expressions in each section are provided in an accompanying MATLAB live script (Data S1), in which we use the MATLAB (The MathWorks, Natick, MA) symbolic toolbox for manipulating the analytical equations.

We note that our assumption throughout this work is that the mechanical response of the interior cytoskeleton can be modeled using continuum CEs. Although these continuum models have been successfully applied to many experiments, there are conditions under which the continuum modeling of stress may start to break down. For example, consider the case in which a handful of microtubules grow sufficiently long to make contact with the cell cortex, whereas the overwhelming majority of them remain confined within a volume surrounding the nucleus. The presence of these few filaments can cause large variations in the motion of the nucleus and the overall mechanics of the cytoskeleton. Such effects that involve small numbers but large variations in the average properties cannot be readily coarse-grained into continuum equations. Mesoscopic simulations are needed to study the mechanical behavior of such systems, which are not pursued in this study.

RESULTS

Nucleus surrounded by a Newtonian fluid

We start by the simplest mechanical model and assume the cytoplasm is a Newtonian fluid of shear viscosity η_o. The nucleus is modeled as a rigid sphere of radius a centered in a spherical cell of radius c; see Fig. 2 a. Because the
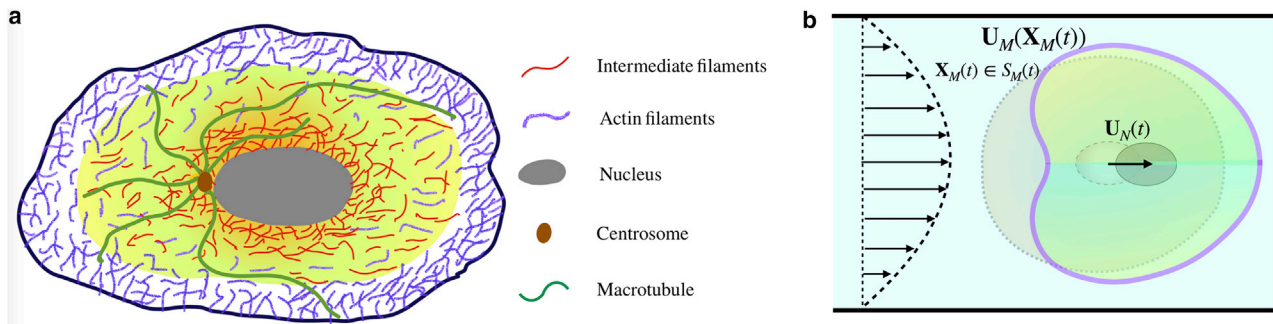

FIGURE 1 (a) A schematic representation of the intracellular assemblies formed by cytoskeletal filaments, namely microtubules, actin filaments, and intermediate filaments. The flexible filaments are either freely suspended or cross-linked and anchored to the nucleus. When the filaments are freely suspended, the cytoplasm behaves as a viscoelastic fluid in the continuum scale. When the filaments are cross-linked, they form a network and behave as a poroelastic material in the continuum scale. (b) A schematic representation of the time-dependent displacements of the cell cortex under external hydrodynamic forces from pressure-driven flows in microchannels and the subsequent displacements of the nucleus, induced by the internal flows generated through the deformations of the cell cortex. Assuming the cortical deformations and hence the surface velocity, U_M, are known through experiments, the nucleus velocity, U_N, can be decoupled from cortex mechanics and fully determined by the surface velocity for a given CE for the cytoplasm. To see this figure in color, go online.
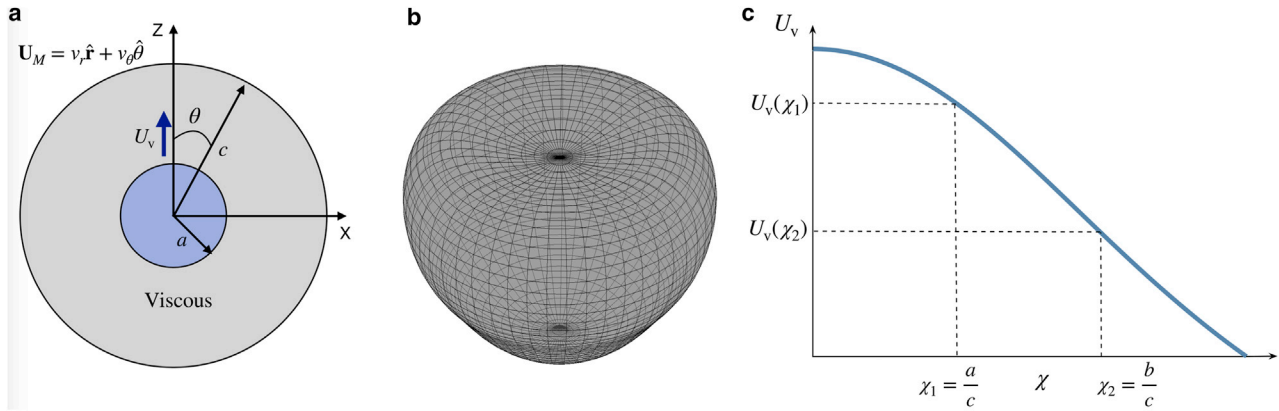
FIGURE 2 (*a*) A force-free spherical nucleus of radius *a* moving with velocity U_v in a Newtonian fluid and confined within a spherical cortex of radius *c*. Because of axisymmetry, the cortex rate of deformations can be decomposed into radial and angular modes of rates of displacement: $v_r = \sum_{n=1}^{\infty} \lambda_n P_n(\cos\theta)$ and $v_\theta = \sum_{n=1}^{\infty} \lambda'_n V_n(\cos\theta)$, where $V_n(\cos\theta) = \frac{2 \sin\theta}{n(n+1)} \frac{dP_n(\cos\theta)}{d\cos\theta}$. (*b*) Outer cell shape for some special values of the first five modes that recapitulates a bullet shape cell: $\lambda_n = [1.0000; -1.1975; -0.8497; -0.8296; -0.2806]$ and $\lambda'_n = [1.0000; 1.7277; 1.3449; -0.8401; 1.8323]$. (*c*) The velocity of the nucleus as a function of the nucleus to the cell cortex radii, $\chi = a/c$, when surface velocity modes are $\lambda_1 = \lambda'_1 = 1$. To see this figure in color, go online.

flow is axisymmetric, the velocity field in spherical coordinates are $\mathbf{v}(r, \theta) = (v_r, v_\theta)$, with $\theta \in [0, \pi]$. The BCs are no slip on cell outer surface, $\mathbf{v}(r = c, \theta)$, and the net velocity of the cell nucleus is $\mathbf{v}(r = a, \theta) = U_v$, where "v" in U_v stands for viscous. Both of these quantities are inputs from experiments. The solutions to radial and angular velocity fields in axisymmetric Stokes flow are given in terms of Legendre polynomials and their derivatives; see Appendix A. Thus, we present the outer surface velocity using the same functions. The additional equation needed to complete the system of equations is the constraint that the nucleus is force free. These conditions are given by the following equations:

$$r = a: \quad v_r = U_v \cos\theta,$$

$$v_\theta = -U_v \sin\theta, \quad \int_{S_a} (\boldsymbol{\sigma} \cdot \mathbf{n}) \cdot \hat{\mathbf{z}} dS = 0 \quad (1a)$$

and

$$r = c: \quad v_r = \sum_{n=1}^{\infty} \lambda_n P_n(\cos\theta), \quad v_\theta = \sum_{n=1}^{\infty} \lambda'_n V_n(\cos\theta),$$
$$(1b)$$

where $V_n(\cos\theta) = \frac{2 \sin\theta}{n(n+1)} \frac{dP_n(\cos\theta)}{d\cos\theta}$ and $P_n(\cos\theta)$ is the Legendre polynomial of order *n*. Note that the choice of $P_n(\cos\theta)$ and $V_n(\cos\theta)$ for radial and angular velocities readily satisfies the incompressibility constraint, $\nabla \cdot \mathbf{v} = 0$.

After applying the BCs, the velocity of the inner sphere is given by

$$U_v = \frac{1}{3}\lambda_1 \left(\frac{6 + 6\chi + \chi^2 + \chi^3 + \chi^4}{1 + \chi + \chi^2 + \chi^3 + \chi^4} \right)$$
$$- \frac{1}{3}\lambda'_1 \left(\frac{-3 - 3\chi + 2\chi^2 + 2\chi^3 + 2\chi^4}{1 + \chi + \chi^2 + \chi^3 + \chi^4} \right), \quad (2)$$

where $\chi = a/c$. This velocity depends on just the first modes of cortex displacement rates and independent of the cytoplasmic viscosity. Fig. 2 *c* shows the velocity of the inner sphere as a function of χ. As a numerical example, if we take $\lambda_1 = \lambda'_1 = 1$, for $\chi = 1/3$, the velocity of the inner sphere is $\frac{959}{363} \approx 2.64$; for $\chi = 2/3$, it is $U_v = \frac{1139}{633} \approx 1.79$; and for $\chi \to 0$, it is $U_v = 2\lambda_1 + \lambda'_1 = 3$.

As we shall see in the next sections, because of the flow axisymmetry, the nucleus velocity only depends on the first surface velocity modes of the cortex, λ_1 and λ'_1, regardless of our choice of model for cytoplasm.

Viscoelastic cytoplasm

Particle-tracking microrheology has been extensively used to measure the linear viscoelastic response of the cytoplasm for many varieties of cells under a wide range of conditions; see (15) and references within for a review on the topic. These studies show that in many cases, the cytoplasm exhibits frequency-dependent storage and loss moduli (15,22,23). However, the type of CE for a given cell type is generally not known. Thus, we use the most general description of a linear viscoelastic incompressible fluid given by

$$\boldsymbol{\sigma}^P(t) = G(t)\boldsymbol{\gamma}(0) + \int_0^t G(t - t')\dot{\boldsymbol{\gamma}}(t') \, \mathrm{d}t', \quad (3)$$

where superscript *p* stands for polymer (filament) phase, $\boldsymbol{\sigma}(t)$ is the stress tensor, $\boldsymbol{\gamma}(t)$ is the strain tensor, $\dot{\boldsymbol{\gamma}}(t) = \partial\boldsymbol{\gamma}/\partial t = \nabla\mathbf{v} + \nabla\mathbf{v}^\mathrm{T}$ is the time-dependent rate of strain tensor, and $G(t)$ is the time-dependent shear modulus. The goal is to determine $G(t)$ as a function of the cell surface and the nucleus velocities.

Intracellular structures in eukaryotic cells are highly heterogeneous. For example, the density of microtubules and intermediate filaments is typically largest near the nucleus and decays toward the outer boundaries; see Fig. 1 a. We model these structural heterogeneities by decomposing the cytoplasm into two domains: we assume that the nucleus of radius a is bound by a spherical shell of outer radius b that contains the viscoelastic fluid. This shell is bounded by a Newtonian fluid that fills the remaining intracellular volume; see the inset of Fig. 3 b. Muñoz et al. used the FIRE imaging technique to probe the morphological changes of *Euglena gracilis* cells—including the intensity and distribution of intracellular lipid droplets and chlorophyll autofluorescence—in response to hydrodynamic

We then use the stream function solution to the Stokes flow in domains I and II and apply BCs in Eqs. 1 and 6 to analytically determine $\tilde{U}(s)$ as a function of surface velocity modes at $r = c$ as

$$\tilde{U}(s) = \frac{1}{3\Delta}\left[\lambda_1(s)\,a_1(\chi_1, \chi_2) + \lambda\prime_1(s)\,b_1(\chi_1, \chi_2)\right.$$
$$\left. + \frac{\tilde{G}(s)}{\eta_\circ}(\lambda_1(s)\,a_2(\chi_1, \chi_2) + \lambda\prime_1(s)\,b_2(\chi_1, \chi_2))\right],$$
(7)

where $\chi_1 = a/c$, $\chi_2 = b/c$, and

$$\Delta = 5\chi_2^5(\chi_1^5 - 1) + \frac{\tilde{G}(s)}{\eta_\circ}(3\chi_2^{10} + 2\chi_2^5\chi_1^5 - 2\chi_1^5 - 3\chi_2^5),$$

$$a_1(\chi_1, \chi_2) = 5\chi_2^5(\chi_1^5 + 5\chi_1^2 - 6), \quad b_1(\chi_1, \chi_2) = 5\chi_2^5(-2\chi_1^5 + 5\chi_1^2 - 3),$$

$$a_2(\chi_1, \chi_2) = 3\chi_2^{10} + 2\chi_1^5\chi_2^5 - 12\chi_1^5 - 18\chi_2^5 + 15\chi_2^7 + 10\chi_1^5\chi_2^2,$$

$$b_2(\chi_1, \chi_2) = -6\chi_2^{10} - 4\chi_1^5\chi_2^5 - 6\chi_1^5 - 9\chi_2^5 + 15\chi_2^7 + 10\chi_1^5\chi_2^2.$$

stresses from flows in microchannels (43). It is reasonable to assume that cytoskeletal filaments can similarly be tagged, and their fluorescent intensity can be used to approximate b.

The total stress within the shell, $a < r < b$, is the sum of the polymeric and cytosol stresses: $\boldsymbol{\sigma} = \eta_\circ \dot{\boldsymbol{\gamma}} + \boldsymbol{\sigma}^p$. Taking Laplace transform of the total stress in time axis and using convolution theorem gives

$$\tilde{\boldsymbol{\sigma}}(s, r, \theta) = \left(\eta_\circ + \tilde{G}(s)\right)(\nabla\tilde{\mathbf{v}}(s, r, \theta) + \nabla\tilde{\mathbf{v}}^T(s, r, \theta)), \quad (4)$$

where superscript $\sim$ denotes variables in Laplace space. Taking the Laplace transform of the momentum equation in the shell and substituting for stress with Eq. 4 results in the Stokes equation in Laplace space

$$\tilde{\eta}\nabla^2\tilde{\mathbf{v}} - \nabla\tilde{p} = 0, \quad a < r < b, \quad (5)$$

where $\tilde{\eta} = (\eta_\circ + \tilde{G}(s))$. Similarly, the momentum equation for outer Newtonian fluid is another Stokes equation with η_o as the shear viscosity. The BCs at the interface, $r = b$, are the continuity of fluid velocity, tangential stress, and pressure, given below:

$$r = b: \quad \tilde{\mathbf{v}}^{(I)} = \tilde{\mathbf{v}}^{(II)}, \quad \tilde{\sigma}_{r\theta}^{(I)} = \tilde{\sigma}_{r\theta}^{(II)}, \quad \tilde{p}^{(I)} = \tilde{p}^{(II)}. \quad (6)$$

Using the experimentally measured velocities of the cell surface and nucleus in Eq. 7, we can compute $\tilde{G}(s)/\eta_o$. This can then be inverted to real space to get $G(t)/\eta_o$. Note that we can only compute $G(t)/\eta_o$ and not the individual variables independently. This is in line with our findings for viscous cytoplasm, in which the nucleus velocity was independent of viscosity and only a function of geometry and the first surface velocity modes. Determining η_o and $G(t)$ separately requires imposing force balance across the cell cortex and specifying a CE for it.

The process of characterizing the linear viscoelastic response from experiments can be summarized as follows:

1) Measure the cell surface and nucleus displacements (and thus velocities) with time and measure the intracellular distribution of filaments by fluorescent microscopy to approximate the outer radius of the shell, $r = b$, in the model.
2) Decompose the cell surface rate of displacements (velocities) in radial and angular directions into Legendre polynomials: $v_r = \sum_{n=1}^{\infty}\lambda_n P_n(\cos\theta)$ and $v_\theta = \sum_{n=1}^{\infty}\lambda_n\prime V_n(\cos\theta)$.
3) Take Laplace transform of the surface velocity models, $\lambda(t)$ and $\lambda\prime(t)$, and the nucleus velocity $U_{VE}(t)$ to get $\tilde{\lambda}(s)$, $\tilde{\lambda}\prime(s)$, and $\tilde{U}(s)$.
4) Use Eq. 7 to compute $\tilde{G}(s)/\eta_o$ and take an inverse Laplace of $\tilde{G}(s)$ to get $G(t)/\eta_o$. To compute the linear
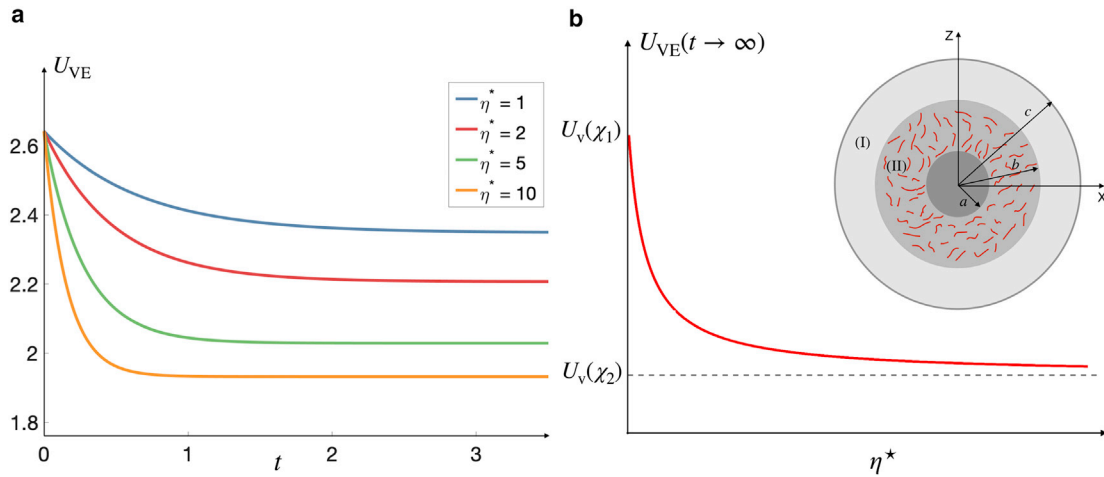
FIGURE 3 (*a*) Velocity of the nucleus as a function of time for different values of the relative viscosity, η^*, in a cytoplasm described by the Maxwell CE when $\chi_1 = 1/3$, $\chi_2 = 2/3$, $\lambda_1 = \lambda_1' = 1$, and $\tau = 1$. (*b*) The long-time velocity of the nucleus moving as a function of the ratio of polymeric/solvent viscosities in the Maxwell CE, $\eta^* = \eta_p/\eta_o$. In the limit of $\eta^* \to 0$, we recover the velocity of a nucleus with radius $r = a$, moving in a Newtonian cytoplasm, $U_v(\chi_1)$; when $\eta^* \to \infty$, we recover the velocity of a nucleus with radius $r = b$ moving in a Newtonian cytoplasm, $U_v(\chi_2)$. Inset: a schematic representation of a viscoelastic shell, adjacent to the nucleus of radius $r = a$ surrounded with a spherical shell of outer radius $r = b$, containing freely suspended flexible filaments. To see this figure in color, go online.

oscillatory functions, $G'(\omega)$ and $G''(\omega)$, one can replace s in $\tilde{G}(s)$ with $i\omega$ and use the expression $G^*(\omega) = i\omega\tilde{G}(i\omega)$ to compute $G^*(\omega)$. The real and imaginary parts of G^* correspond to G' and G'', respectively.

The experimental inputs, including $\lambda(t)$, $\lambda'(t)$, and $U(t)$, contain certain levels of uncertainty (error) due to the limitations of optical and fluorescent microscopy. The question that may arise is how sensitive are the predictions to these experimental uncertainties? We have studied this effect through a series of numerical experiments by adding white noises of relative amplitudes up to 0.4 to $\lambda(t)$, $\lambda'(t)$, and $U(t)$. The predictions of constitutive coefficients in the presence of white noise were within 10% of the results obtained in the absence of any noise, indicating that the method can be applied to noisy data without significant loss of accuracy. The details of these numerical experiments are outlined in Appendix C.

Thus far, we have outlined how experimentally provided values of $U_{VE}(t)$ and $\lambda(t)$ and $\lambda'(t)$ can be used to compute the linear rheology of the cytoplasm. In the next section, we use the simplest viscoelastic CE, namely a Maxwell fluid, to explore the role of geometrical parameters (such as χ_2) and physical parameters (such as the relaxation time τ) on the time-dependent response of U_{VE}.

We note that the rheology of cytoplasm is far more complex than a Maxwell fluid. The consensus that emerges from a large number of careful experimental studies of the linear viscoelastic properties of the cytoskeleton from various groups and using different rheological characterization techniques is that the storage and loss moduli commonly follow a power-law dependency with frequency (44). This implies that the cytoskeleton rheology is determined by the integral

effect of multiple processes that span a wide range of time-scales. This power-law behavior can be understood using the framework of soft glassy materials (45,46) and fractional calculus (47,48).

The model consistent with the mentioned studies describes the dynamic moduli by a sum of two power laws (9):

$$G'(\omega) = A \cos(\pi\beta/2)\omega^\beta + B \cos(3\pi/8)\omega^{3/4} \quad (8a)$$

and

$$G''(\omega) = A \sin(\pi\beta/2)\omega^\beta + B \sin(3\pi/8)\omega^{3/4}, \quad (8b)$$

where $0.15 < \beta < 0.25$ and A and B are constants dependent on the biological system. Given that we have an analytical form for $G'(\omega)$ and $G''(\omega)$, we can compute $\tilde{G}(s)$ using the transformation $G^*(\omega) = i\omega\tilde{G}(i\omega)$ and substitute it into Eq. 7. Assuming that $U(t)$, $\lambda(t)$, and $\lambda'(t)$ are known from experiment, we can follow the same four steps laid out before to compute the exponent β that minimizes the difference between the predicted and experimentally measured values of the nucleus velocity. For brevity and simplicity, we do not discuss the results of this class of CEs in the main text. We do, however, present the predictions of the CE given by Eqs. 8a and 8b in the accompanying Data S1.

Example: Maxwell fluid

We model the fluid within the shell using a Maxwell CE, which is given by

$$\left(1 + \tau\frac{\partial}{\partial t}\right)\boldsymbol{\sigma}^p = \eta_p\mathbf{D}. \quad (9)$$

Here, $\tau = \eta_p/G_p$ is the relaxation time of the polymer phase, and η_p and G_p are the shear viscosity and modulus of the polymer phase. Although the nucleus velocity can be computed for any time-dependent choice of functions $\lambda(t)$ and $\lambda'(t)$, we choose the simplest case of constant velocity modes $\lambda = \lambda' = 1$. This choice provides an analogy to creep and stress relaxation experiments in shear rheology. Taking the Laplace transform of the shell stress and the surface velocities gives $\tilde{G}(s) = \frac{\eta_p}{1+s\tau}$ and $\tilde{\lambda} = \tilde{\lambda}' = \frac{1}{s}$. We can compute the nucleus velocity in Laplace space by substituting for $\tilde{G}(s)$, $\tilde{\lambda}(s)$, and $\tilde{\lambda}'(s)$ in Eq. 7. Inverting from Laplace to time space gives

$$U_{\mathrm{VE}}(t) = f_1(\chi_1, \chi_2, \eta^\star)\lambda_1 + f_2(\chi_1, \chi_2, \eta^\star)\lambda_1' \\ + (\lambda_1 + \lambda_1')f_3(\chi_1, \chi_2, \eta^\star)e^{-t/\tau_{\mathrm{VE}}}, \quad (10)$$

where $\eta^* = \frac{\eta_p}{\eta_\circ}$ and

$$f_1 = \frac{1}{\Delta}\left(5\chi_1^5\chi_2^5 - 30\chi_2^5 + 25\chi_1^2\chi_2^5 + \eta^\star\left(3\chi_2^{10} + 2\chi_1^5\chi_2^5 - 12\chi_1^5 - 18\chi_2^5 + 15\chi_2^7 + 10\chi_1^5\chi_2^2\right)\right),$$

$$f_2 = \frac{1}{\Delta}\left(-10\chi_1^5\chi_2^5 - 15\chi_2^5 + 25\chi_1^2\chi_2^5 + \eta^\star\left(-6\chi_2^{10} - 4\chi_1^5\chi_2^5 - 6\chi_1^5 - 9\chi_2^5 + 15\chi_2^7 + 10\chi_1^5\chi_2^2\right)\right),$$

$$\text{and } f_3 = \frac{5\eta^\star(1-\chi_2)(2\chi_1^6 - 2\chi_1^5\chi_2 + 3\chi_1\chi_2^5 - 3\chi_2^6)}{\Delta(1 + \chi_1 + \chi_1^2 + \chi_1^3 + \chi_1^4)} \times$$

$$(\chi_1^3\chi_2 + \chi_1^3 + \chi_1^2 + \chi_1 + \chi_1^2\chi_2^2 + \chi_1\chi_2^3 + \chi_2^3 + \chi_2^2 + \chi_2 + 2\chi_1\chi_2(1 + \chi_1 + \chi_2)),$$

with $\Delta = 3(5\chi_1^5\chi_2^5 - 5\chi_2^5 + \eta^\star(3\chi_2^{10} + 2\chi_1^5\chi_2^5 - 2\chi_1^5 - 3\chi_2^5))$ and

$$\tau_{\mathrm{VE}} = \tau\frac{5\chi_2^2(1 - \chi_1^5)}{5\chi_2^2(1 - \chi_1^5) + \eta^\star((1 - \chi_2^5)(3\chi_2^5 + 2\chi_1^5))}. \quad (11)$$

Fig. 3 a shows the velocity of the inner sphere as a function of time for $a = 1$, $b = 2$, $c = 3$, $\lambda_1 = 1$, and $\lambda_1' = 1$. At $t = 0$, $\sigma_p = 0$, and the velocity of the nucleus is that of a solid sphere of radius $r = a$ in a Newtonian fluid with viscosity η_o. At long times, the steady-state velocity of the nucleus is a function of relative viscosity, η^*. The limit of $\eta^* = 0$ corresponds to negligible contribution to stress from the polymeric phase, and we recover the velocity of the inner sphere for a Newtonian fluid with viscosity η_o. In the limit of $\eta_p \to \infty$, the outer shell behaves asymptotically as a solid sphere; thus, the nucleus velocity asymptotes to the velocity of a nucleus with radius $r = b$ in a Newtonian fluid of viscosity η_o (see Fig. 3 b). Thus, η^* can be determined by the long-time (small frequency) values of the nucleus velocity, and the relaxation time can be determined by its intermediate values.

Next, we consider periodic deformations of the cell cortex as an analogy to linear oscillatory shear rheology. Unlike the case of constant values of λ and λ', periodic deformations can be experimentally realized, e.g., by periodic regions of contractions and expansion; see Fig. 4 a for a schematic. A wide range of frequencies and magnitude of these deformations can, in principle, be explored by tuning the external fluid viscosity, flow rate, and geometrical features of the microchannel. If we assume that the cortex (cell surface) displacements are sinusoidal with frequency ω, namely $\lambda = \lambda_o\cos\omega t$, we expect the nucleus velocity to have a frequency-dependent phase lag (δ) in response to these surface deformations, $U_{\mathrm{VE}}(t) = U_{\mathrm{VE}}^0\cos(\omega t + \delta)$. For purely viscous fluid, this phase lag, δ, is identically zero. Thus, plotting $U_{\mathrm{VE}}(t)$ vs. $\lambda(t)$ and $\lambda'(t)$ will produce a line. For a linear viscoelastic fluid, $0 < \delta < \pi/2$, and $U_{\mathrm{VE}}(t)$ vs. $\lambda(t)$ and $\lambda'(t)$ curves would be tilted ellipses.

These curves are known as Lissajous curves in rheology, and they provide a powerful tool for nonlinear rheological fingerprinting of complex fluids using large amplitude (nonlinear) oscillatory rheology (49). Although we have limited our analysis to linear regime, $U_{\mathrm{VE}} - \lambda_n$ curves and the mathematical framework developed to analyze these curves can, in practice, be deployed to characterize the linear and nonlinear viscoelastic behavior of the cytoplasm over a wide range of forces and frequencies. As an example, Fig. 4 b shows $U_{\mathrm{VE}}(t)$ vs. $\lambda_1(t) = \lambda_1'(t) = \cos\omega t$ at different frequencies using Eq. 7. We see that the area within the tilted ellipse is increased and decreased, showing complex rheological response of the system. In linear shear oscillatory rheology, the geometric properties of this curve, such as the area within the ellipse and its maxima, can be used to extract $G'(\omega)$ and G'' (49). Analogous relationships can be derived in our case using Eq. 7, which relates the curve characteristics to material parameters such as $G(t)/\eta_o$. However, one important difference with the shear rheology is that in our case, these relationships will also be dependent on the details of fluid flow geometry, i.e., χ_1 and χ_2. We will not derive these relationships here.
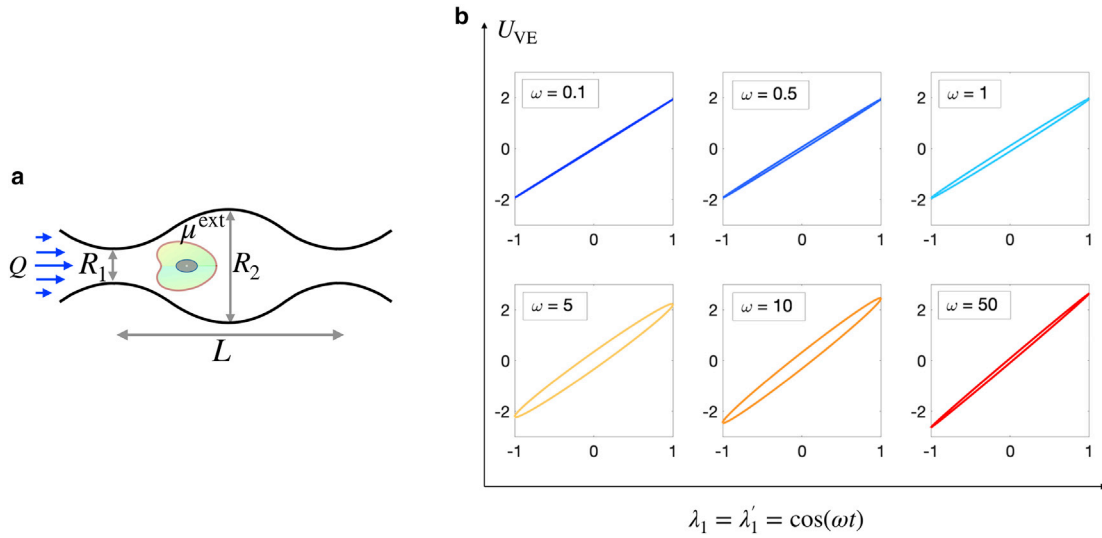
FIGURE 4 (*a*) A schematic representation of a cell moving through a microchannels with periodic contractions and expansions. This periodicity in geometry results in periodic external hydrodynamic forces and cell deformations. The frequency and amplitude of these deformations can, in principle, be controlled through changing the microchannels geometry (R_1, R_2, and L), as well as the fluid viscosity and flow rate (μ^{ext} and Q). (*b*) Velocity of the nucleus versus the velocity of the cortex for periodic deformation of the cortex, $\lambda_1 = \lambda_1' = \cos(\omega t)$, at different frequencies ω when the cytoplasm is described by the Maxwell CE with relaxation time $\tau = 1$ and $\eta^* = 10$. To see this figure in color, go online.

Special case of $\chi_2 = 1$

For the special case of the shell extending all the way to the cell surface, $\chi_2 = 1$, the velocity of the nucleus becomes independent of $\tilde{G}(s)$, and the coefficients in Eq. 7 are $\Delta = 5(\chi_1^5 - 1)$, $a_1 = 5(\chi_1^5 + 5\chi_1^2 - 6)$, $b_1 = 5(-2\chi_1^5 + 5\chi_1^2 - 3)$, and $a_2 = b_2 = 0$. Thus,

$$\tilde{U}(s) = \frac{1}{3\Delta}[\lambda_1(s)\,a_1(\chi_1) + \lambda\prime_1(s)\,b_1(\chi_1)]. \quad (12)$$

For constant first modes $\lambda_1(s) = \lambda'_1(s) = \frac{1}{s}$, this velocity is equal to the velocity of nucleus in viscous medium, and we recover Eq. 2. Hence, structural heterogeneity within the cytoplasm must be present to observe the nontrivial nucleus velocities discussed here. This special case is physiologically improbable because the cytoskeletal organizations are almost always heterogeneously distributed. Conversely, this analysis also points to the importance of accounting for these heterogeneities in our models.

Porous shell

Thus far, we have described the cytoplasm mechanics, using a general linear viscoelastic CE to model the presence of the cytoskeletal assemblies. The underlying assumption in this coarse graining is that the net force on each filament, and the filament phase as a whole, is identically zero. The force moment on the filaments, however, is nonzero, giving rise to an extra stress in the continuum limit, which is modeled through the appropriate CEs.

The force-free condition for filaments is valid as long as they are freely suspended, with no constraint in their motion. In cytoskeletal assemblies, the filaments are often cross-linked together or to other structures via motor proteins and passive cross-linkers. In other words, the filaments form networks rather than suspensions. For example, microtubules typically nucleate from microtubule organizing centers, which are attached to the nuclear envelope; see Fig. 1 *a*. Thus, the microtubule array and the nucleus move together. Because of the constrains in their motion, the filaments (microtubules) experience a net drag force due to the relative motion of the cytoplasmic fluid with respect to the network (array).

On the continuum scale, this force can be modeled through a body force acting on the network. This force scales linearly with the velocity difference between the network and the fluid phases, $\mathbf{f}^{porous}(\mathbf{x}) \sim (\mathbf{v}(\mathbf{x}) - \mathbf{U})$. In other words, the filament network around the nucleus behaves as a porous medium. In the first step, we neglect the elastic properties of the network and assume the network is made of rigid filaments with uniform orientation and density. Assuming that the cytoplasmic fluid permeating the network is Newtonian, the fluid flow within the network can be modeled using the Brinkman equation:

$$a < r < b: \quad \eta_\circ \nabla^2 \mathbf{v} - \frac{\eta_\circ}{\kappa}\mathbf{v} - \nabla p = 0 \quad \text{and} \quad \nabla \cdot \mathbf{v} = 0,$$
$$(13)$$

where $\kappa = 1/\alpha^2$ is the permeability of the medium. Note that in Eq. 13, the velocity field, $\mathbf{v}(\mathbf{x})$, is defined in the

coordinates that move with the nucleus such that $\mathbf{v}(\mathbf{x}) = 0$ when $\mathbf{x} \in S_a$.

Here, we provide a simple scaling analysis of the fluid permeation in cytoskeletal networks. The volume fraction of these networks within the cytoplasm is typically small, $\phi \ll 1$. Sangani and Acrivos (50) give an asymptotic expression for permeability:

$$\frac{\kappa}{a_f^2} = \frac{1}{8\phi}(-\ln \phi - 1.48), \tag{14}$$

where a_f is the radius of the filament. From this expression, we see that because $\phi \ll 1$, the fluid permeability is large in the length scale of the filament radius, $\kappa/a_f^2 \gg 1$. For microtubules, which have the largest radius among cytoskeletal filaments, $a_f \approx 12$ nm. As a result, the ratio of nucleus/filament radius is typically $\mathscr{O}(10^3)$. Rescaling this expression to the nucleus radius, which is the scale of interest here, gives $\frac{\kappa}{a^2} = \left(\frac{a_f}{a}\right)^2 \frac{1}{8\phi}(-\ln \phi - 1.48)$. Even for very small volume fractions, we have the likely condition of $\phi(a/a_f)^2 \gg 1$, which makes $\kappa/a^2 \leq 1$, resulting in substantial reduction in fluid permeability by the network in the nucleus (and the cell) length scale. In other words, the network can have large effects on the fluid flows and the nucleus dynamics even when $\phi \ll 1$.

Here, we consider a porous cytoplasm with a rigid nucleus in a concentric spherical geometry; see Fig. 5 a. Because the flow is axisymmetric, the velocity field in spherical coordinates would be $\mathbf{v}(r, \theta) = (v_r, v_\theta)$, with $\theta \in [0, \pi]$. The BCs and the force-free condition in the nucleus are given by

$$v_r^{(\mathrm{II})} = -\left(A\prime_2 + \frac{B\prime_2}{r^3} + \frac{C\prime_2}{r^2}y_2(\alpha r) + \frac{D\prime_2}{r^2}y_{-2}(\alpha r)\right)\cos\theta \text{ and}$$

$$v_\theta^{(\mathrm{II})} = \left(A\prime_2 - \frac{1}{2}\frac{B\prime_2}{r^3} + \frac{C\prime_2}{2r}y_2{}'(\alpha r) + \frac{D\prime_2}{2r}y_{-2}{}'(\alpha r)\right)\sin\theta, \tag{16}$$

where $y_2(\alpha r) = \alpha\cosh(\alpha r) - \frac{1}{r}\sinh(\alpha r)$ and $y_{-2}(\alpha r) = \alpha\sin(\alpha r) - \frac{1}{r}\cosh(\alpha r)$. For general n, $y_n(\alpha r)$ and $y_{-n}(\alpha r)$ are proportional to modified Bessel functions of the first and second kinds, respectively.

The fluid adjacent to the shell (domain I) is modeled as a Stokesian fluid:

$$v_r^{(\mathrm{I})} = -\left(A_2 + \frac{B_2}{r^3} + C_2 r^2 + \frac{D_2}{r}\right)\cos \theta \text{ and}$$

$$v_\theta^{(\mathrm{I})} = \left(A_2 - \frac{1}{2}\frac{B_2}{r^3} + 2C_2 r^2 + \frac{1}{2}\frac{D_2}{r}\right)\sin \theta. \tag{17}$$

The force on the nucleus is expressed as

$$F = 2\pi b^2 \int_0^\pi [\sigma_{rr} \sin \theta - \sigma_{r\theta} \cos \theta]|_{r=b} \sin \theta \, d\theta$$

$$= 6\pi\eta \, U_\mathrm{B} b \left(\frac{2}{3}D_2\sqrt{\kappa} \,\Big/\, b\right). \tag{18}$$

Imposing force-free conditions, $F = 0$, sets $D_2 = 0$. The remaining unknown coefficients are determined by imposing BCs in Eqs. 15. The resulting nucleus velocity,

$$r = a: \quad \mathbf{v}^{(\mathrm{II})} = 0, \quad \int_{S_a}(\boldsymbol{\sigma} \cdot \mathbf{n}) \cdot \widehat{\mathbf{z}} = 0,$$

$$r = b: \quad \mathbf{v}^{(\mathrm{I})} = \mathbf{v}^{(\mathrm{II})} \quad \sigma_{r\theta}^{(\mathrm{I})} = \sigma_{r\theta}^{(\mathrm{II})}, \quad p^{(\mathrm{I})} = p^{(\mathrm{II})}, \text{ and} \tag{15}$$

$$r = c: \quad v_r^{(\mathrm{I})} = -U_\mathrm{B} \cos \theta + \sum_{n=1}^{\infty}\lambda_n P_n(\cos \theta), \quad v_\theta^{(\mathrm{I})} = -U_\mathrm{B} \sin \theta + \sum_{n=1}^{\infty}\lambda_n{}' V_n(\cos \theta),$$

where $V_n(\cos\theta =)\frac{2\sin\theta}{n(n+1)}\frac{dP_n(\cos\theta)}{d(\cos\theta)}$ and $P_n(\cos\theta)$ are Legendre polynomials and the subscript B of U denotes Brinkman. Similar to the Stokes equation, one can find the general solution to axisymmetric flows from the Brinkman equation. The explicit form of the stream function and the equations for the velocity and stress components are provided in Appendix A. We apply the BCs using axisymmetric stream functions of the Stokes and Brinkman equations for domains (I) and (II), respectively; see Fig. 5 a. The velocity components for the first mode in the Brinkman domain are

U_B, is then calculated analytically as a function of permeability, geometrical parameters $\chi_1 = a/c$ and $\chi_2 = b/c$, and the first surface velocity modes λ_1 and $\lambda_1{}'$. The final expression for U_B runs a few pages long and is not produced here but is given in Data S1. Fig. 5 b shows U_B vs. $\alpha = \sqrt{1/\kappa}$ for different values of shell thickness (χ_2) when $\lambda_1 = \lambda_1{}' = 1$ and $\chi_1 = 1/3$. In the limit of $\alpha \to 0$, the fluid permeates the shell without any resistance and U_B asymptotes to the velocity of the Newtonian fluid of $\chi = \chi_1$. On the other hand, in the limit of $\alpha \to \infty$, the fluid cannot
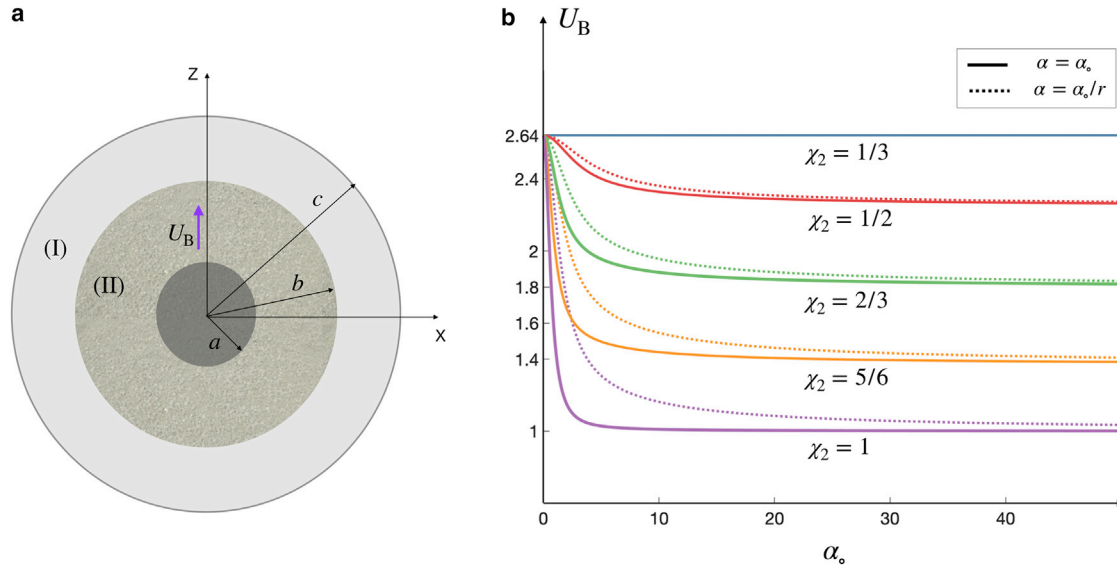
FIGURE 5 (a) A schematic representation of a porous shell of outer radius $r = b$, surrounding the nucleus of radius $r = a$. The shell is composed of filaments anchored to the nucleus and cross-linked together. (b) Velocity of the nucleus as a function of $\alpha_o = 1/\sqrt{\kappa}$ for different values of $\chi_2 = b/c$. The dashed line shows the same results for spatially variant permeability $\alpha = \alpha_o/r$, where r is the distance from the center of the nucleus. As expected, at a given α_o the average permeability of the radially decaying α is less than the constant permeability case, leading to larger values for the nucleus velocity. The limiting values at $\alpha_o \to 0$ and $\alpha_o \to \infty$ are identical for both constant and spatially variant permeability and correspond to the nucleus velocity in a Newtonian cytoplasm with inner and outer radii $r = a$ and $r = b$: $U_v(\chi_1)$ and $U_v(\chi_2)$, respectively. To see this figure in color, go online.

permeate the shell, and U_B asymptotes to the velocity of the Newtonian fluid of $\chi = \chi_2$.

Spatially varying permeability

As discussed earlier, the cytoskeletal structures are heterogeneously distributed in space. As an example, microtubules nucleate from microtubule organizing centers and emanate radially toward the cell boundary; see Fig. 1 a. As a result, their number density decays as they grow outwards. Assuming the same length for all microtubules, the volume fraction (or number density) decays as $\phi = \phi_o/r^2$. Considering $\kappa^{-1} \sim \phi$ when $\phi << 1$ (see Eq. 14), we get $\kappa = \kappa_o r^2$, which modifies the Brinkman equation to

$$\eta_\circ \nabla^2 \mathbf{v} - \frac{\eta_\circ}{\kappa_\circ r^2}\mathbf{v} - \nabla p = 0. \tag{19}$$

In this particular case, the modified Brinkman equation allows simple analytical solutions, which are outlined in Appendix A. These solutions are subjected to the same BCs as the constant permeability given in Eq. 15 to compute the nucleus velocity as a function of λ, λ', χ_1, χ_2, and α_o.

Fig. 5 b compares the results of U_B as a function of $\alpha_o = 1/\sqrt{\kappa_\circ}$, when $\alpha = \alpha_o/r$ with the results of constant α of the same value as α_o when $\chi_1 = 1/3$, $\chi_2 = 2/3$, and $\lambda_1 = \lambda_1' = 1$. As expected, the values of α corresponding to the same value of U_B are larger for radially decaying α (increasing permeability).

Poroelastic shell

Finally, we consider the case in which the surrounding shell, $a < r < b$, is a two-phase mixture composed of a deformable viscoelastic network of filaments and a Newtonian fluid permeating it. The momentum and mass balance equations of these two phases, when $\phi << 1$, are given by

$$\nabla \cdot \boldsymbol{\sigma}_f + \frac{\eta_\circ}{\kappa}\left(\mathbf{v}_n - \mathbf{v}_f\right) = 0; \quad \nabla \cdot \mathbf{v}_f = 0 \tag{20}$$

and

$$\nabla \cdot \boldsymbol{\sigma}_n + \frac{\eta_\circ}{\kappa}\left(\mathbf{v}_f - \mathbf{v}_n\right) = 0, \quad \frac{\partial \phi}{\partial t} + \nabla \cdot (\phi \mathbf{v}_n) = 0, \tag{21}$$

where $\boldsymbol{\sigma}_f = \eta_0(\nabla \mathbf{v}_f + \nabla \mathbf{v}_f^T) - p_f \mathbf{I}$ and $\boldsymbol{\sigma}_n$ are fluid and network total stress tensors, each averaged over their associated phases, and ϕ is the volume fraction of filaments. The CE for a linear viscoelastic and isotropic network is given by

$$\boldsymbol{\sigma}_n = \int_0^t \left[G(t-t')\left(\nabla \mathbf{v}_n(t') + \nabla \mathbf{v}_n^T(t')\right) \right.$$
$$\left. + \left(K(t-t') - \frac{2}{3}G(t-t')\right)(\nabla \cdot \mathbf{v}_n(t'))\mathbf{I} \right] dt', \tag{22}$$

where G and K are the time-dependent shear and bulk moduli of the network and $\mathbf{v}_n = \frac{d\mathbf{u}_n}{dt}$ is the rate of displacement of the network phase.

Because the permeability is a function of the local volume fraction of filaments (in the limit of $\phi \ll 1$, $\kappa^{-1} \sim \phi$), the mass and momentum are coupled, leading to a system of nonlinear partial differential equations. These equations, subject to the appropriate BCs, can be solved numerically. But finding analytical solutions for them seems out of reach. For simplicity and analytical tractability, we assume that the volume fraction of the network remains uniform in space and time: $\frac{D\phi}{Dt} = \partial\phi/\partial t + \mathbf{v}_n \cdot \nabla\phi = 0$. Applying these assumptions reduces the network mass balance to $\nabla \cdot \mathbf{v}_n = 0$. This constraint can only be imposed, without overdetermining of our system, when $K \to \infty$ (see Eq. 22). In this limit, in the exact manner as the Navier-Stokes equations, we would have $(K - 2G/3)(\nabla \cdot \mathbf{v}_n) = -p_n$, where p_n is the pressure in the network phase and a Lagrange multiplier to impose incompressibility of the network phase. Applying these considerations and taking a Laplace transform of Eq. 22 yields

$$\tilde{\boldsymbol{\sigma}}_n = \tilde{G}(s)\left(\nabla\tilde{\mathbf{v}}_n + \nabla\tilde{\mathbf{v}}_n^T\right) - \tilde{p}_n\mathbf{I}. \tag{23}$$

Next, we take a Laplace transform of Eq. 21 and substitute for $\tilde{\sigma}_n$ using Eq. 23. The resulting equations are

$$\eta_\circ\nabla^2\tilde{\mathbf{v}}_f - \nabla\tilde{p}_f + \frac{\eta_\circ}{\kappa}\left(\tilde{\mathbf{v}}_n - \tilde{\mathbf{v}}_f\right) = 0 \tag{24}$$

and

$$\tilde{G}(s)\nabla^2\tilde{\mathbf{v}}_n - \nabla\tilde{p}_n + \frac{\eta_\circ}{\kappa}\left(\tilde{\mathbf{v}}_f - \tilde{\mathbf{v}}_n\right) = 0. \tag{25}$$

Summation and subtraction of Eqs. 24 and 25 lead to

$$\eta_\circ\nabla^2\tilde{\mathbf{v}}^+ - \nabla\tilde{p}^+ = 0 \tag{26}$$

and

$$\eta_\circ\nabla^2\tilde{\mathbf{v}}^- - \nabla\tilde{p}^- - \frac{\eta_\circ}{\tilde{\kappa}}\tilde{\mathbf{v}}^- = 0, \tag{27}$$

where $\tilde{p}^+ = \tilde{p}_f + \tilde{p}_n$, $\tilde{p}^- = \tilde{p}_f - \tau(s)\tilde{p}_n$, and

$$\tau(s) = \frac{\eta_\circ}{\tilde{G}(s)}, \quad \tilde{\mathbf{v}}^+ = \tilde{\mathbf{v}}_f + \frac{\tilde{\mathbf{v}}_n}{\tau(s)}, \quad \tilde{\mathbf{v}}^- = \tilde{\mathbf{v}}_f - \tilde{\mathbf{v}}_n, \quad \text{and} \quad \frac{1}{\tilde{\kappa}}$$

$$= \frac{1}{\kappa}\left(1 + \tau(s)\right).$$

Note that $\tilde{\mathbf{v}}^+$ and $\tilde{\mathbf{v}}^-$ satisfy the Stokes and Brinkman equations, respectively, for which we have analytical expressions for the velocity and stress fields. The BCs for the nucleus at $r = a$ and $r = c$ are identical to those provided for the Brinkman, viscoelastic, and Newtonian fluid cases. The BCs at the interface, $r = b$, are the continuity of fluid velocity, tangential stress, and pressure (corresponding to

continuity of force across the boundary) for the fluid phase and zero pressure and tangential stress for the network phase (zero force on the outer network boundary):

$$r = b: \quad \tilde{\mathbf{v}}^{(I)} = \tilde{\mathbf{v}}_f^{(II)}, \quad \tilde{\sigma}_{r\theta}^{(I)} = \tilde{\sigma}_{f,r\theta}^{(II)}, \quad \tilde{p}^{(I)} = \tilde{p}_f^{(II)}, \quad \tilde{\sigma}_{n,r\theta}^{(II)}$$
$$= 0, \quad \tilde{p}_n^{(II)} = 0. \tag{28}$$

These BCs can be written in terms of $\tilde{\mathbf{v}}^+$ and $\tilde{\mathbf{v}}^-$ by using $\tilde{\mathbf{v}}_f = \frac{\tau\tilde{\mathbf{v}}^+ + \tilde{\mathbf{v}}^-}{\tau+1}$ and $\tilde{\mathbf{v}}_n = \frac{\tau(\tilde{\mathbf{v}}^+ - \tilde{\mathbf{v}}^-)}{\tau+1}$. The modified equations are

$$r = a: \quad \tilde{\mathbf{v}}^+ = 0, \quad \tilde{\mathbf{v}}^- = 0 \tag{29a}$$

and

$$r = b: \quad \tilde{\mathbf{v}}^{(I)} = \frac{\tau\tilde{\mathbf{v}}^+ + \tilde{\mathbf{v}}^-}{\tau + 1}, \quad \tilde{\sigma}_{r\theta}^{(I)} = \tilde{\sigma}_{r\theta}^+, \quad \tilde{p}^{(I)}$$
$$= \tilde{p}^+, \quad \tilde{\sigma}_{r\theta}^+ - \tilde{\sigma}_{r\theta}^- = 0, \quad \tilde{p}^+ - \tilde{p}^- = 0. \tag{29b}$$

We then use the stream function solution to the Stokes and Brinkman flows in domains I and II and apply BCs in Eqs. 1 and 29 to analytically determine $U_{PE}(s)$ as a function of χ_1, χ_2, λ_1, λ'_1, κ, η_o, and $\tau(s)$. Similar to the case of porous media, the final expression for U_{PE} is very lengthy and is only given in Data S1.

We can use the computed expression for U_{PE} and follow the same four steps outlined in Viscoelastic cytoplasm to compute κ and $\eta_o/G(t) = \tau(t)$. Similarly, we can compute $G'(\omega)/\eta_o$ and $G''(\omega)/\eta_o$ using $G^*(\omega) = G'(\omega) + iG^*(\omega) = i\omega\tilde{G}(i\omega)$. Below, we discuss the results for the simplest model of a network, namely the linear isotropic elastic model. We present the variations of U_{PE} as a function of geometric parameters, including χ_2, and physical parameters, including κ. Our aim for choosing this simple and physically inaccurate representation of the cytoskeleton mechanics is to highlight the effect of simple geometrical and physical parameters such as χ_2, κ, and τ on the time-dependent response of the nucleus. However, in Data S1, we reproduce the results presented in the next section for a more physically accurate choice of the CE of cytoskeletal assemblies given by Eq. 8.

Example: linear elastic network

We model the network mechanics using a linear isotropic, elastic model, in which $\tau = \eta_o/G$ is a constant.

Fig. 6 a shows the velocity of the nucleus versus time for different values of $\alpha_o = \sqrt{1/\kappa}$ at $\tau = 1$, and Fig. 6 b shows the time-dependent nucleus velocity for different values of τ at $\alpha_o = 1$. Also, we take $\chi_1 = 1/3$, $\chi_2 = 2/3$, and $\lambda_1 = \lambda_1' = 1$. As can be seen, the initial velocity, $U_{PE}(t = 0)$, is independent of α_o and τ. At short times, the network deformation, and hence its drag force against the fluid flow, is small. Thus, the fluid permeates the network without resistance, and the nucleus velocity asymptotes to the velocity obtained
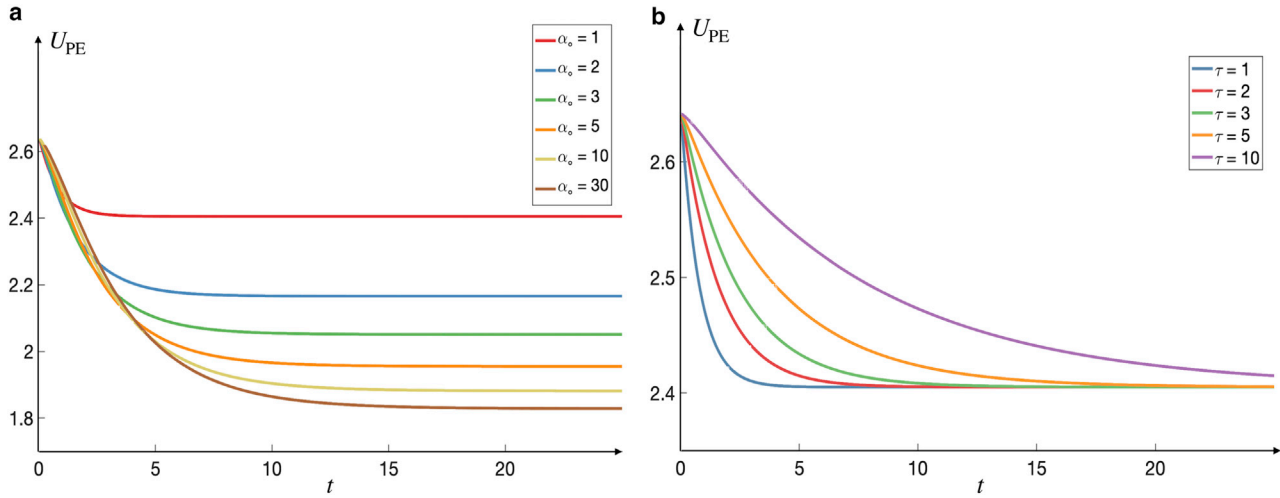
FIGURE 6 (*a*) Velocity of the nucleus as a function of time for different values of permeability, α_o, and a fixed value of elastic relaxation time, $\tau = 1$. At short ($t \rightarrow 0$) and long ($t \rightarrow \infty$) times, the velocity asymptotes to $U_v(\chi_1)$ and $U_B(\alpha_o, \chi_1, \chi_2)$, respectively. (*b*) Velocity of the nucleus versus time for different values of elastic relaxation time τ and a fixed permeability $\alpha_o = 1$, when $\chi_1 = 1/3$, $\chi_2 = 2/3$, and $\lambda_1 = \lambda_1' = 1$. To see this figure in color, go online.

for a Newtonian fluid with $\chi = \chi_1$. We confirm this analytically by using the relationship

$$\lim_{s \rightarrow \infty} s \, \tilde{U}_{PE}(s) = \lim_{t \rightarrow 0} U_{PE}(t) = U_v(\chi_1).$$

On the other hand, at long times, network deformation reaches its steady state, and $\mathbf{v}_n \rightarrow U_{PE}\hat{\mathbf{z}}$. In this limit, the momentum equation reduces to the Brinkman equation: $U_{PE} \rightarrow U_B(\chi_1, \chi_2, \alpha_o)$. We confirm this relationship by evaluating the following limit of $\tilde{U}_{PE}$:

$$\lim_{s \rightarrow 0} s \, \tilde{U}_{PE}(s) = \lim_{t \rightarrow \infty} U_{PE}(t) = U_B(\chi_1, \chi_2, \alpha_o).$$

At the intermediate times, the nucleus velocity approaches its steady-state value with an effective relaxation time that is a function of both τ and α_o. An equation of form $y = y_i + (y_e - y_i)\exp(-t/\tau)$ fits the data presented in both figures very well. Given that we know the limiting values of $U_{PE}(t)$ at $t = 0$ and $t \rightarrow \infty$, $U_{VE}(t)$ can be approximated using the following general form:

$$U_{PE}(t) = U_v(\chi_1)$$
$$+ (U_B(\chi_1, \chi_2, \alpha_o) - U_v(\chi_1))\exp\left[-\frac{t}{\tau_{PE}^{\star}(\tau, \alpha_o, \chi_1, \chi_2)}\right],$$

(30)

where $\tau_{PE}^{\star}$ is the relaxation timescale that depends on geometric parameters, as well as τ and α_o.

Fig. 7 *a* shows the value of poroelastic timescale as a function of permeability. As can be seen, $\tau_{PE}^{\star}/\tau$ monotonically increases (decreases) with α_o (κ_o) and approaches a constant that is independent of τ and only a function of χ_1 and χ_2 as the shell becomes impermeable ($\alpha_o \rightarrow \infty$).

Because the exponential expression is an approximation to our solution, it is difficult to extract analytical expressions for $\tau_{PE}^{\star}$ for general values of α_o, τ, χ_1, and χ_2. We can, however, obtain exact expressions for the nucleus velocity in the limit of nearly zero permeability, $\alpha_o \rightarrow \infty$. The expression is a combination of two exponential relaxations for constant values of λ_1 and λ_1':

$$U_{PE} = U_v(\chi_2) + (\lambda_1 + \lambda_1')\left[f_1(\chi_1, \chi_2)e^{-\frac{t}{\tau}} + f_2(\chi_1, \chi_2)e^{-\frac{t}{\tau^{\star}}}\right],$$

$$\tau^{\star} = \tau\left(\frac{15\chi_2^5(1 - \chi_1^5)}{(1 - \chi_2^5)(2\chi_1^5 + 10\chi_1^2\chi_2^3 + 3\chi_2^5)}\right),$$

(31)

where $f_1(\chi_1, \chi_2)$ and $f_2(\chi_1, \chi_2)$ are lengthy geometric functions and are given in Appendix B. One of these relaxation times is simply the relaxation time of the network, τ, and the other one, τ^*, is proportional to τ and a function of geometry. Given that $b/a \geq 1$, $\tau^* \geq \tau$. For example, for the choice of $\chi_1 = 1/3$ and $\chi_2 = 2/3$, we have $\tau^* = 3.1\tau$, which corresponds to the solid line shown in the inset of Fig. 7 *a*. As expected, in the limit of $t \rightarrow \infty$, the nucleus velocity asymptotes to the velocity of a nucleus with radius $r = b$ in a Newtonian fluid, $U_v(\chi_2)$.

Next, we compute the velocity of the nucleus for the case in which the permeability is proportional to the square of the distance, $\kappa = \kappa_o r^2 \Rightarrow \alpha = \frac{\alpha_o}{r}$; see Fig. 7, *c* and *d*. Following the same steps as the case of constant permeability, we arrive at two equations for $\tilde{\mathbf{v}}^+$ and $\tilde{\mathbf{v}}^-$:

$$\eta_o \nabla^2 \tilde{\mathbf{v}}^+ - \nabla \tilde{p}^+ = 0$$

(32)

and

$$\eta_\circ \nabla^2 \tilde{\mathbf{v}}^- - \nabla \tilde{p}^- - \frac{\eta_\circ}{\kappa_\circ r^2} \tilde{\mathbf{v}}^- = 0. \qquad (33)$$

Similar to the case of constant permeability, $\tilde{\mathbf{v}}^+$ satisfies the Stokes equation and the equation for $\tilde{\mathbf{v}}^-$ is the modified Brinkman equation with variable permeability, $\alpha = \alpha_\circ/r$. The analytical solution for the modified Brinkman equation is outlined in Appendix A. The unknown coefficients in stream function solutions for Stokes and modified Brinkman equations are then determined by imposing BCs given by Eq. 29.

Fig. 7 c shows the variations of the nucleus velocity with time for different values of $\alpha_\circ$ when the permeability is spatially variant, $\alpha = \alpha_\circ/r$, and the choice of $\chi_1 = 1/3$, $\chi_2 = 2/3$, and $\tau = 1$. The behavior is qualitatively similar to the case of constant permeability shown in Fig. 6 a. Variations of normalized effective relaxation time $\tau_{\mathrm{PE}}^\star/\tau$ vs. $\alpha_\circ$ for a radially decaying $\alpha = \alpha_\circ/r$ is shown in Fig. 7 d for two choices of χ_1 and χ_2. The inset figure in Fig. 7 c shows the variations of $\tau_{\mathrm{PE}}^\star/\tau$ vs. χ_2 for different values of $\alpha_\circ$ when $\chi_1 = 1/3$. Again, in both cases, the results are qualitatively similar to the constant permeability case shown in Fig. 7 a.

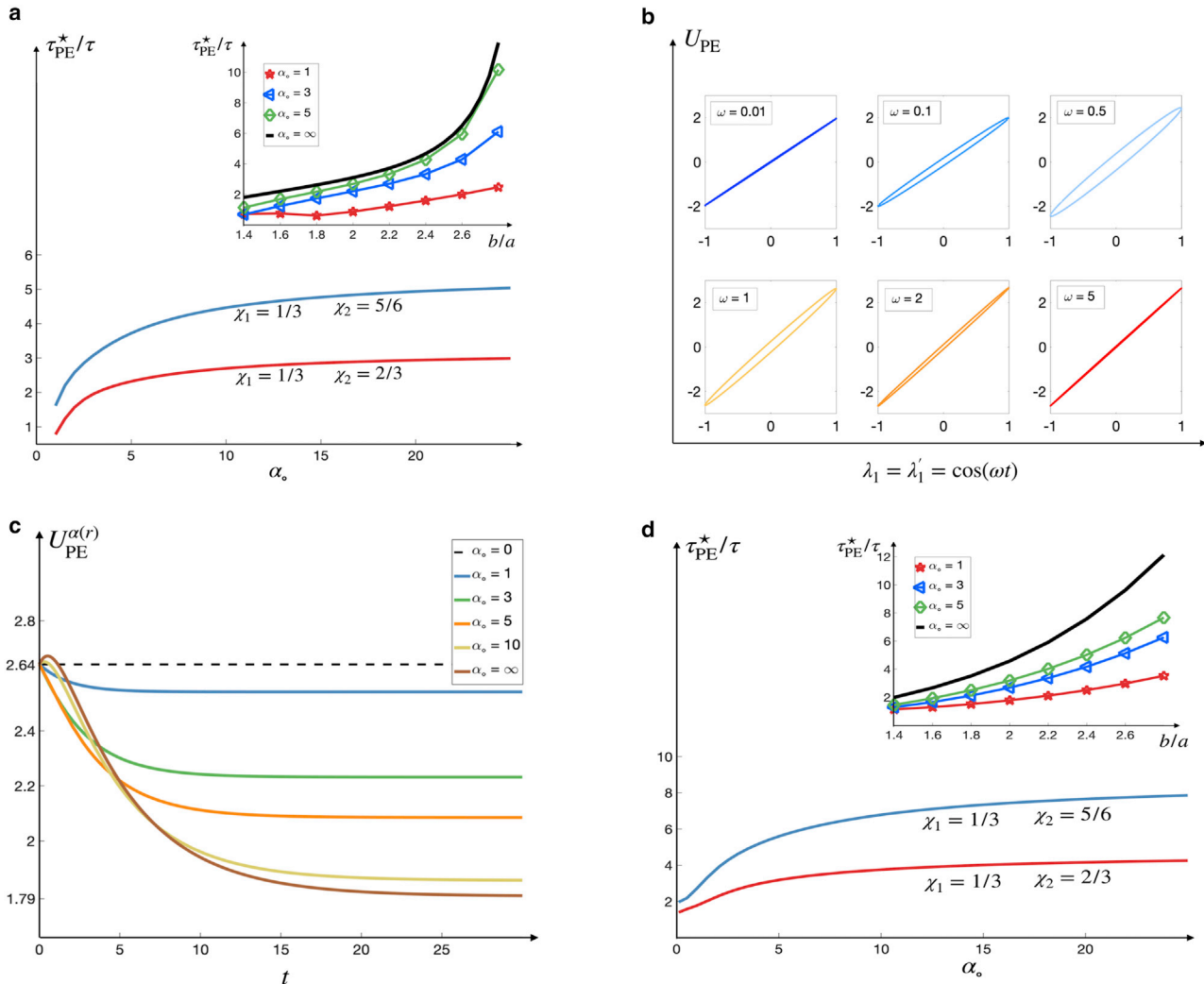FIGURE 7 (*a*) Normalized poroelastic relaxation time, $\tau_{\mathrm{PE}}^\star/\tau$, as a function of permeability $\alpha_\circ$ for two different values of poroelastic shell size χ_2, where $\tau_{\mathrm{PE}}^\star$ is computed by fitting Eq. 30 on the results of $U_{\mathrm{PE}}(t)$ vs t. Note that all the effective relaxation times, τ^*, for different values of τ collapse to a single curve once they are normalized by τ. Inset: normalized poroelastic timescale as a function of the ratio of the shell to the nucleus radii, b/a, for different values of $\alpha_\circ$. The solid line corresponds to the limit of $\alpha_\circ \to \infty$, given by Eq. 31. (*b*) Velocity of the nucleus versus the membrane velocity for a poroelastic shell when membrane deformations are periodic: $\lambda_1 = \lambda_1' = \cos(\omega t)$. The results are reported for $\chi_1 = 1/3$, $\chi_2 = 2/3$, and different rate of deformation frequencies ω. The curves at small and large frequencies, corresponding to long and short timescales, asymptote to linear curves signifying nearly viscous behaviors. At intermediate frequencies (timescales), the nucleus velocity has a frequency-dependent phase lag (δ), $U_{\mathrm{PE}}(t) = U_{\mathrm{PE}}^0\cos(\omega t + \delta)$, signifying a viscoelastic response. These phase lags result in tilted ellipse shapes when plotting U_{PE} vs. λ and λ'. (*c*) Velocity of the nucleus as a function of time for a poroelastic cytoplasm with variable permeability, $\alpha = \alpha_\circ/r$, when $\chi_1 = 1/3$, $\chi_2 = 2/3$, and $\lambda_1 = \lambda_1' = 1$. (*d*) Normalized poroelastic relaxation time in variable permeability case, $\alpha(r) = \alpha_\circ/r$, as a function of $\alpha_\circ$ for two different shell outer radii, $\chi_2 = 2/3$ and $\chi_2 = 5/6$. Inset: normalized poroelastic timescale as a function of the ratio of the shell to the nucleus radii, b/a, for different permeabilities. To see this figure in color, go online.

Special case of $\chi_2 = 1$

Thus far, we have assumed that the poroelastic network that surrounds the nucleus does not fill the entire cytoplasm, $b < c$, i.e., the filaments that make the network do not make mechanical contact with the cell cortex. This assumption may not hold in many physiological conditions. For example, during cell division, many astral microtubules polymerize or depolymerize against the cell cortex and generate forces that are key for positioning the mitotic spindle (51). In this limit, the filaments (microtubules) make contact with the cortex, and any displacement of the cortex results in their deformation. Therefore, the force acting on the outer surface of the poroelastic network phase is no longer zero, and simply evaluating the expressions of the previous section in the limit of $b \rightarrow c$ will give the wrong results.

What are the correct BCs for the outer surface of the network at $r = c$? The choice depends on the details of micromechanical interactions of the filaments with the outer boundary. We consider two scenarios. In scenario I, we assume the filaments remain mechanically attached to the cell cortex as it deforms. This can occur, for example, if the filament ends are mechanically trapped in the dense cortical actin network. In this scenario, the network displacements will be equal to the cortical displacements.

In scenario II, we assume that the filaments cannot penetrate out of the cell boundary, i.e., the network and the cortical displacements are equal in the direction normal to the cell boundary. However, we assume the filaments can bend and slide tangentially without any frictional resistance from the cellular boundary; see Fig. 8 *a* for a schematic of both scenarios. The BCs for scenarios I and II are

$$\text{scenario I}: \quad v_{n,r} = \sum_{n=1} \lambda_n P_n(\cos\theta), \quad v_{n,\theta}$$

$$= \sum_{n=1} \lambda'_n V_n(\cos\theta) \tag{34a}$$

and

$$\text{scenario II}: \quad v_{n,r} = \sum_{n=1} \lambda_n P_n(\cos\theta), \quad \sigma_{n,r\theta} = 0. \tag{34b}$$

We then solve Eq. 27 subject to the no-slip BCs for the fluid and network phase at $r = a$ and the BCs given in Eqs. 34a and 34b rewritten in terms of $\tilde{v}^+$ and $\tilde{v}^-$ for both scenarios. We find that in scenario I, the nucleus velocity is simply given by $U = U_v(\chi_1)$.

The behavior is more complex and time dependent in scenario II. Fig. 8 *b* shows the nucleus velocity versus time for different values of constant permeability α_o in scenario II, when $\lambda_1 = \lambda'_1 = 1$, $\chi_1 = 1/3$, and $\tau = 1$. The inset shows the effective normalized relaxation time versus α_o for different nucleus radii (χ_1). As a comparison, in Fig. 8 *c*

we show the results of Fig. 8 *b* when we use the expressions for a poroelastic shell in the limit of $b \rightarrow c$ to compute the nucleus velocity versus time. We can see that the predictions are qualitatively different from scenario II, underscoring the important role of micromechanical interactions and BCs in the limit in which the network is in direct contact with the cell cortex.

In reality, the cortex-network interactions may likely be a combination of scenario I and II and the case of no contact (shell model), which also makes the nucleus velocity a combination of all these three ideal conditions. We model the transition between the two limits of scenarios I and II by including a tangential frictional force applied by the boundary to the sliding filaments. As a result, the BC of the network phase in θ direction modifies to

$$\text{mixed scenarios I and II}: \quad \sigma_{n,r\theta} = -k(v_{n,\theta} - v_{f,\theta}), \tag{35}$$

where k is the friction coefficient and the BC in radial directions remains unchanged. These BCs are then transformed to *s*-space and presented in terms of $\tilde{v}^+$ and $\tilde{v}^-$. Fig. 8 *d* shows the predictions of the nucleus velocity with time using the same parameters as Fig. 8 *b* for different values of k while keeping $\alpha_o = 1$. As expected, at $k = 0$ we recover the results of scenario II, whereas for $k \rightarrow \infty$, the nucleus velocity asymptotes to a constant value, as predicted by scenario I. The inset figure shows the variations of effective relaxation time of the network as a function of α_o for different values of k. Note that the choice of k changes the steady-state (long-time) behavior of the network, and increasing k reduces the effective relaxation time; see the inset of Fig. 8 *d*.

CONCLUSIONS

Cell mechanics is a powerful tool for studying structural changes in different cellular processes. Cell populations and their mechanical properties are highly heterogeneous from cell to cell and from one location of the cell to the next. Thus, measurements need to be conducted for large number of cells. This constraint severely limits application of several techniques such as atomic force microscopy and particle-tracking microrheology, especially for clinical applications. Using hydrodynamic forces in microfluidic platforms to deform cells is by far the highest-throughput technique (thousands of cells per second) and the most suitable for applications involving detecting and characterizing rare cell populations in clinical samples. Despite their remarkable success, the previous mechanical characterizations of cells in microchannels are limited in one fundamental way; they largely use a single static measure of deformability as the metric for characterizing the mechanics. Therefore, it is very difficult to measure the
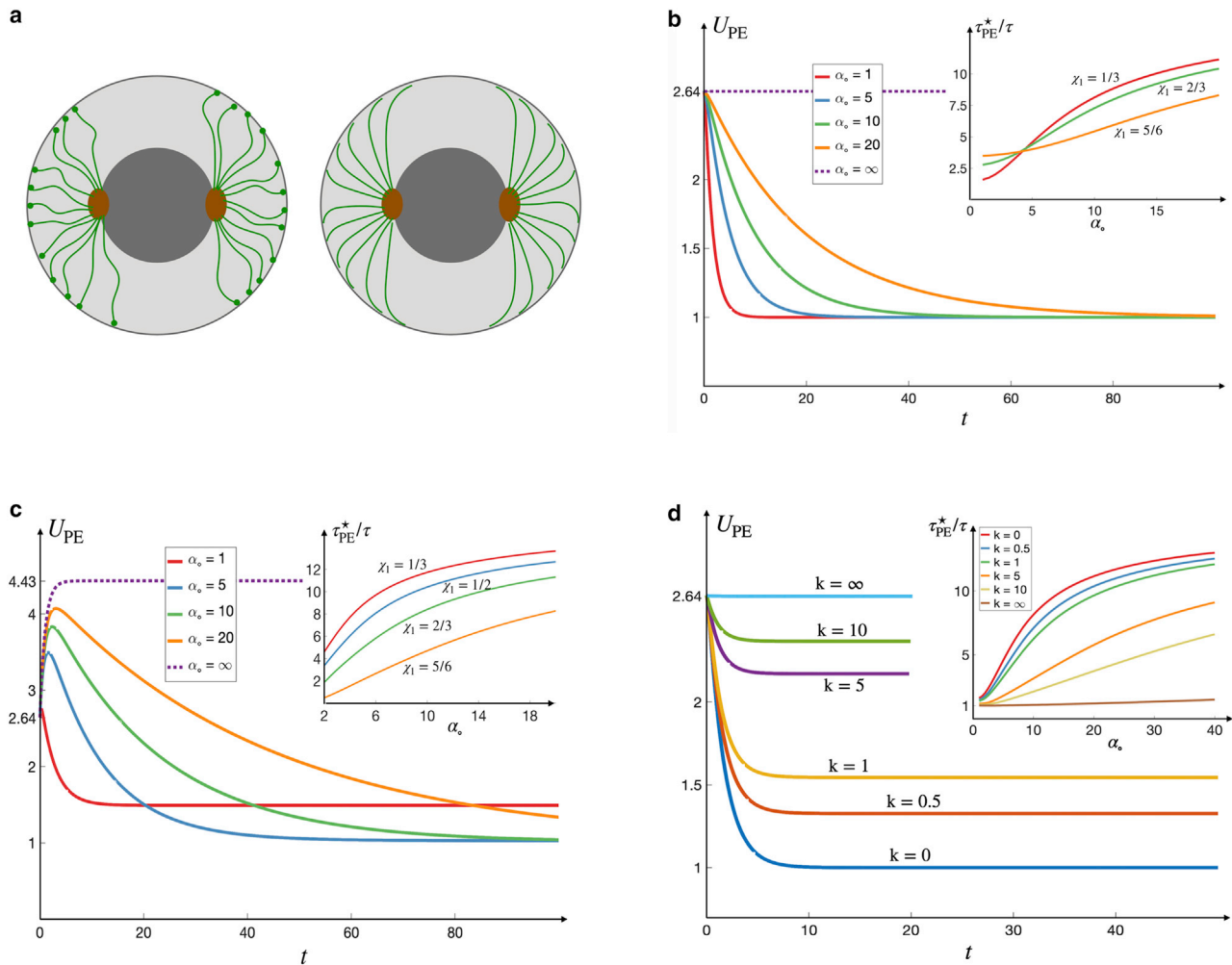
FIGURE 8 (*a*) Schematic representations of scenario I (*left*), in which the filament ends are mechanically trapped on the cell's cortical network and, as a result, normal and tangential network displacements or velocities are equal to those of the cell cortex, and scenario II (*right*), in which the network filaments cannot penetrate the cell cortex (excluded volume) but can bend and slide tangential to the boundary without resistance. Thus, network displacement or velocity equals that of the cell cortex in the direction normal to the surface (no penetration), and the tangential component of the network stress vanishes (free sliding). (*b*) Velocity of the nucleus as a function of time in scenario II for different values of α_o when $\chi_1 = 1/3$, $\lambda_1 = \lambda_1' = 1$, and $\tau = 1$. Inset: normalized effective relaxation time in scenario II versus α_o for different nucleus radii χ_1. (*c*) Velocity of the nucleus as a function of time for a poroelastic spherical shell, where the BCs are the continuity of normal and tangential stress at the interface $r = b$, when $b \rightarrow c$. Inset: normalized effective poroelastic relaxation time as a function of permeability for different nucleus radii χ_1. (*d*) The nucleus velocity versus time for the mixed scenarios I and II, in which the BC at $r = c$ and tangential direction is modified to $\sigma_{n,r\theta} = -k(v_{n,\theta} - v_{f,\theta})$. The results are presented for $\chi_1 = 1/3$, $\lambda_1 = \lambda_1' = 1$, $\tau = 1$, and $\alpha_o = 1$ and different values of friction coefficient k. As expected, at k = 0 we recover the results of scenario II, whereas for k $\rightarrow \infty$, the nucleus velocity asymptotes to a constant value, as predicted by scenario I. The inset figure shows the variations of effective relaxation time of the network as a function of α_o for different values of k. Note that the choice of k changes the steady-state (long-time) behavior of the network and that the effective relaxation time is decreased with increasing k. To see this figure in color, go online.

contribution of different structural components of the cell—including the cell nucleus, the cytoplasm, and the cell membrane—to the mechanics of the whole cell. This is particularly important because different processes and diseases are known to target different cellular structures. Moreover, numerous studies show that cell rheology is time dependent, which is not included in previous modeling studies of deforming cells in microchannels.

One major barrier in overcoming these limitations has been the lack of sufficient imaging resolution to probe the time-dependent displacements. In the past decade, there have been remarkable advancements in high-speed fluorescent and optical imaging and their integration into microfluidic platforms. Because of these advancements, we can now tag and track cellular boundaries and different components within the cells as they flow through microchannels (10,36–38) with high spatial and temporal resolution. Yet there is no theoretical framework that enables utilizing these data to measure the time-dependent rheology of different cellular components.

This work introduces a computational method that makes use of this type of data to measure the rheology of the cell cytoplasm and its immersed cytoskeleton over a wide range of timescales. As a model system, we considered a spherical cell with a centered spherical nucleus. We assumed that the cell deformations and the nucleus displacements are sufficiently small that the nucleus remains centered and the cell remains spherical during the deformations. In these conditions, the interior flow remains axisymmetric, and the nucleus velocity can be computed analytically. Below, we summarize the main contributions of this method.

1) Decoupling the rheology of the cell cortex from the cytoplasm: as we discussed earlier, one standing challenge in studying cell mechanics is to determine the relative contribution of different cellular structure to the whole-cell response measured in microfluidic experiments. We have proposed a novel, to our knowledge, method to measure the rheology of cytoplasm, without the need to include the mechanics of the cell cortex. The underlying assumption in all the calculations presented here is that velocity of the cell cortex is known from experiments through tracking the boundary. In this case, the internal flows and deformations can be fully determined by the cell cortex velocity and the rheology of the cytoplasm, without the knowledge of the forces acting on the boundary and the mechanics of the cortex.

2) Explicitly accounting for the cell nucleus and using it as a microrheological probe: unlike previous studies in which the cell interior was modeled as a single-phase material, we have modeled the cell interior as the composition of the nucleus and the cytosol with its immersed cytoskeleton, which we refer to as the cytoplasm. Considering that the nucleus is by far the stiffest structure inside the cell, we have modeled it as a rigid sphere.

   The nucleus moves in response to the cell's interior flows induced by cortical deformations. The relationship between nucleus and surface velocities is determined by the rheology of the cytoplasm. Here, we assume that the nucleus displacement can be experimentally measured, which can then be used to characterize the rheology of the cytoplasm. Thus, including the nucleus not only provides a more accurate description of the cell's interior, it can also be used as a microrheological probe to characterize the rheology of the cytoplasm.

   Nuclear mechanics can, however, be more complex, with these complexities playing a key role in many cellular processes. For example, growing evidence over the past decade suggests that the nucleus is a mechanosensory unit of the cell (52). Also, the nuclear composition, and thus mechanics, is known to be grossly affected by disease processes (52,53). Moreover, cell migration through tight extracellular environments may induce large deformations of the nucleus, which

can have large effects on their migration timescales (54). As we learn more about the multicomponent nuclear organization, composite mechanical models, such as the ones presented here, can be constructed and applied to study the force transmission from the cell membrane to the cytoplasm, nuclear envelope, and nucleoplasm and the effects of these forces on chromosome organization.

3) Accounting for the cell's structural heterogeneity: the density of cytoskeletal filaments such as microtubules can vary greatly within the cell. To account for this, we have divided the cytoplasm into two volumes: a shell surrounding the nucleus, where filaments like microtubules are localized, and the remaining volume surrounding the shell, which we modeled as a Newtonian fluid. The shape and dimensions of these localized regions of filaments can, in practice, be visualized with the proper fluorescent tags for the relevant cytoskeletal filaments. We showed that including these structural heterogeneities can lead to qualitative changes in the nucleus dynamics.

4) Assuming time-dependent rheology for the cytoplasm: previous modeling studies of cell deformation in microchannels model the cell as an elastic capsule or an elastic membrane filled with Newtonian fluid (17,18). These models do not capture the complex time-dependent response of the cell (44). In this study, we used four different rheological models for the shell surrounding the nucleus. In the first step, we modeled the entire cytoplasm as a Newtonian fluid. The nucleus velocity can be described in terms of the first modes of the cell's radial and angular surface velocities, once they are decomposed into Legendre polynomials. The nucleus velocity in this case was only a function of the ratio of the nucleus to cell radii and independent of the viscosity of the cytoplasm; see Eq. 2.

   Next, we modeled the shell as a general linear viscoelastic fluid. Taking a Laplace transform of the time coordinate modifies the momentum equation to the Stokes equation with an s-dependent viscosity; see Eq. 5. The analytical solution to this equation provides an expression that relates the experimentally measured displacements of the nucleus and the cell cortex to the time-dependent shear modulus; see Eq. 7.

   As an example, we explored the predictions of the model when the fluid is described by Maxwell's equation. We considered constant and sinusoidal surface velocities, as analogs to creep/stress relaxation and linear oscillatory experiments in shear rheology. Note, however, that the formulation is applicable to any time-dependent form of surface velocities; see Fig. 4. We provided an analytical expression for the relaxation time of the nucleus velocity (see Eq. 11) as a function of the ratio of the radii of the nucleus and viscoelastic shell surrounding it to the cell radius, χ_1 and χ_2, and

ratio of the viscosity of the filament phase to the cytosol, η^*.

- Viscous and viscoelastic CEs are most suitable for modeling force-free suspensions of cytoskeletal filaments. Because in most cytoskeletal assemblies, the filaments are cross-linked, their motions are constrained. In such conditions, the cytoplasm is more accurately described as a porous (rigid filaments) or a poroelastic (flexible filaments) medium. We first modeled the shell as a porous medium and used Brinkman equation to model the fluid flows within it. These equations were solved analytically subject to the appropriate BCs to give the nucleus velocity as a function of cytoplasm permeability, κ, and geometric parameters, χ_1 and χ_2; see Fig. 5. Thus, measuring the cell's surface and the nucleus velocities allows for computing the shell permeability.

- Next, we modeled the shell as a poroelastic medium composed of a viscoelastic network and a Newtonian fluid phase; see Eqs. 21, 22, and 23. Through Laplace transform and a few simple changes of variables, these equations were rewritten as Stokes and Brinkman equations in s-space; see Eq. 27. These equations were solved analytically to express the nucleus velocity as a function of the cell surface velocities, the geometric parameters χ_1 and χ_2, the viscoelastic properties of the network, and its permeability κ. Similar to the case of viscoelastic shells, this expression can be used to compute the viscoelastic response of the network as well its permeability.

- As an example, we considered the case of a linear elastic network and studied the effect of geometrical factors χ_1 and χ_2, as well as the network relaxation time τ and permeability κ on the predicted nucleus velocity; see Figs. 7 and 8. Our results show that the relaxation timescale of the nucleus velocity is proportional to τ and changes significantly with κ, χ_1, and χ_2.

Our results also show that both viscoelastic and poroelastic models produce qualitatively similar predictions of the nucleus velocity for a given $\lambda(t)$ and $\lambda'(t)$, which raises the question of how can one differentiate between these two classes of models? We recall that the viscoelastic CE models a suspension of freely floating filaments and its long-time response is viscous, whereas the long-time response of the poroelastic CE is elastic-like. Thus, one possible method to choose the appropriate model is to track the overall shape or displacement field of the tagged cytoskeletal assembly. In the poroelastic model, we expect the tagged region to undergo finite deformations, whereas in the viscoelastic model, we expect to observe the mixing of filamentous regions because of the generated flows.

As discussed in the main text, relating the surface velocities to the nucleus velocity only allows us to compute the relaxation times of the cytoplasm and not its viscosity.

Determining the viscosity requires knowing the traction on the interior side of cell cortex, $\mathbf{f}_I$. On the other hand, because the viscosity of fluid in microchannels is known, we can compute the traction applied on the outer surface of the cell, $\mathbf{f}_O$, by solving the Stokes equation (or Navier-Stokes in case inertial forces are important), subject to no-slip BCs on the surface. Force balance across the interface gives $\mathbf{f}_I + \mathbf{f}_O + \mathbf{f}_M = 0$, which means that the interior traction can only be determined if the membrane traction is known. Thus, determining the viscosity of cytoplasm requires coupling the mechanics of the membrane (cortex) with the interior flows. We are currently working on extending our method to the case of the spherical cell moving in cylindrical channel, for which the exterior flow can be computed analytically.

As mentioned, the aim of this study was to demonstrate the utility of such a modeling approach for characterizing the time-dependent rheology of the cytoplasm. Thus, we made several simplifying assumptions—which may not necessarily hold in the experimental and physiological conditions—to obtain analytical expressions for the nucleus velocity. These assumptions include modeling the cell and the nucleus as spheres and that the cell deformations are sufficiently small that 1) the cell remains spherical, 2) the nucleus remains roughly centered, and 3) the material time derivatives appearing in viscoelastic CEs can be approximated by partial derivatives: $D/Dt \approx \partial/\partial t$. These assumptions can certainly be relaxed, which would necessitate solving the equations numerically.

APPENDIX A: A STREAM FUNCTION SOLUTION FOR STOKES AND BRINKMAN EQUATIONS

Stokes equation stream function

The Stokes and continuity equations are given by

$$\eta\nabla^2\mathbf{v} - \nabla p = 0 \quad \text{and} \quad \nabla \cdot \mathbf{v} = 0. \tag{36}$$

Because the flow is axisymmetric, we have $v_\phi = 0$ and $\partial/\partial\phi = 0$ where $\phi \in [0, 2\pi]$ and $\mathbf{v}(r, \theta) = (v_r, v_\theta)$ with $\theta \in [0, \pi]$. The velocity components are expressed in terms of the Stokes stream function in spherical coordinates by

$$
\begin{aligned}
v_r &= -\frac{1}{r^2\sin\theta}\frac{\partial\psi}{\partial\theta} \\
v_\theta &= \frac{1}{r\sin\theta}\frac{\partial\psi}{\partial r},
\end{aligned}
\tag{37}
$$

where ψ satisfies the following differential equation:

$$E^4\psi = E^2\left(E^2\psi\right) = 0, \quad E^2 = \frac{\partial^2}{\partial r^2} + \frac{\sin\theta}{r^2}\frac{\partial}{\partial\theta}\left(\frac{1}{\sin\theta}\frac{\partial}{\partial\theta}\right). \tag{38}$$

The general solution to the stream function is (55)

$$\psi(r,\theta) = \sum_{n=2} \left(A_n r^n + B_n r^{-n+1} + C_n r^{n+2} + D_n r^{-n+3} \right)$$
$$\times \mathscr{G}_n^{-1/2}(\cos\theta),$$
(39)

where $\mathscr{G}_n^{-1/2}(\cos\theta)$ are Gegenbauer polynomials defined as $\mathscr{G}_n^{-1/2}(\cos\theta) := \frac{1}{2n-1}(P_{n-2}(\cos\theta) - P_n(\cos\theta))$ and $P_n(\cos\theta)$ is the Legendre polynomial of degree n. Using Eq. 39 and $\frac{d\mathscr{G}_n^{-1/2}(\cos\theta)}{d(\cos\theta)} = -P_{n-1}(\cos\theta)$ modifies Eq. 38 to

$$v_r = -\sum_{n=2} \left(A_n r^{n-2} + B_n r^{-n-1} + C_n r^n \right.$$
$$\left. + D_n r^{-n+1} \right) P_{n-1}(\cos\theta)$$
(40)

and

$$v_\theta = \sum_{n=2} \left(n A_n r^{n-2} + (-n+1)B_n r^{-n-1} + (n+2)C_n r^n \right.$$
$$\left. + (-n+3)D_n r^{-n+1} \right) \frac{\mathscr{G}_n^{-1/2}(\cos\theta)}{\sin\theta}.$$
(41)

Accordingly, the fluid stress components and the pressure are given by

$$\sigma_{rr}^{H} = 2\eta \sum_{n=2} \left[(2-n)\frac{A_n}{r^{3-n}} + (n+1)\frac{B_n}{r^{n+2}} \right.$$
$$\left. + \frac{-n^2+3n+1}{n-1}\frac{C_n}{r^{-n+1}} + \frac{n^2+n-3}{n}\frac{D_n}{r^n} \right] P_{n-1}(\cos\theta),$$
(42)

$$\sigma_{r\theta}^{H} = 2\eta \sum_{n=2} \left[\frac{2-n}{n-1}\frac{A_n}{r^{3-n}} - \frac{n+1}{n}\frac{B_n}{r^{n+2}} - \frac{n+1}{n}\frac{C_n}{r^{-n+1}} \right.$$
$$\left. - \frac{n-2}{n-1}\frac{D_n}{r^n} \right] \frac{dP_{n-1}(\cos\theta)}{d\theta},$$
(43)

and

$$p^{H} = -2\eta \sum_{n=2} \left[\frac{2n+1}{n-1}\frac{C_n}{r^{-n+1}} + \frac{2n-3}{n}\frac{D_n}{r^n} \right] P_{n-1}(\cos\theta).$$
(44)

Stream function for Brinkman equation with constant permeability

The Brinkman equation for a porous medium and the continuity equation are

$$\eta\nabla^2\mathbf{v} - \eta\alpha^2\mathbf{v} - \nabla p = 0 \quad \text{and} \quad \nabla\cdot\mathbf{v} = 0,$$
(45)

where $\alpha = 1/\sqrt{\kappa}$ and κ is the permeability. The stream function for constant permeability, $\alpha = \alpha_0$, satisfies the following differential equation:

$$E^4\psi^\star - \alpha_\circ^2\left(E^2\psi^\star\right) = 0.$$
(46)

Solutions of the above equation may be obtained by setting $\psi^* = \psi^{(1)} + \psi^{(2)}$, where ψ_1 and ψ_2 satisfy the following differential equations:

$$\left(E^2 - \alpha_\circ^2\right)\psi^{(1)} = 0,$$
(47a)

$$\left(E^2 - \alpha_\circ^2\right)\psi^{(2)} = W,$$
(47b)

and

$$E^2 W = 0.$$
(47c)

The solution for $\psi^{(2)}$ is $\psi^{(2)} = -\frac{1}{\alpha_\circ^2}W$, which is $(a_n r^n + b_n r^{-n+1})\mathscr{G}_n(\cos\theta)$. The solution for $\psi^{(1)}$ is obtained by separation of variables, $\psi^{(1)} = R(r)Z(\xi)$, which upon substitution yields $(\xi = \cos(\theta))$

$$r^2\frac{d^2R}{dr^2} - n(n-1)R - \alpha_\circ^2 r^2 R = 0$$
(48a)

and

$$\left(1-\xi^2\right)\frac{d^2Z}{d\xi^2} + n(n-1)Z = 0.$$
(48b)

The latter equation is the Gegenbauer equation with degree $-1/2$. By change of variable $R = \sqrt{r}R_1$, the differential equation for R_1 transforms to the modified Bessel differential equation

$$r^2\frac{d^2R_1}{dr^2} + r\frac{dR_1}{dr} - \left(\left(n-\frac{1}{2}\right)^2 + \alpha_\circ^2 r^2\right)R_1 = 0.$$
(49)

Thus, the general solution for the stream function of the Brinkman fluids is given by

$$\psi^\star(r,\theta) = \sum_{n=2} \left[\tilde{A}_n r^n + \tilde{B}_n r^{(-n+1)} + \tilde{C}_n y_n(\alpha_\circ r) \right.$$
$$\left. + \tilde{D}_n y_{-n}(\alpha_\circ r) \right] \mathscr{G}_n^{-1/2}(\cos\theta).$$
(50)

Here, $\alpha_o = 1/\sqrt{\kappa}$, and $y_n(\alpha_o r)$ and $y_{-n}(\alpha_o r)$ are related to the modified Bessel function as

$$y_n(\alpha_\circ r) = \sqrt{\frac{\pi\alpha_\circ r}{2}}\alpha_\circ^{n-\frac{1}{2}}\,I_{n-\frac{1}{2}}(\alpha_\circ r),\ y_{-n}(\alpha_\circ r)$$

$$= \sqrt{\frac{\pi\alpha_\circ r}{2}}\alpha_\circ^{n-\frac{1}{2}}\,I_{-\left(n-\frac{1}{2}\right)}(\alpha_\circ r). \tag{51}$$

For $n = 2$, $y_2(\alpha_o r) = \alpha_o\cosh(\alpha_o r) - \frac{1}{r}\sinh(\alpha_o r)$ and $y_{-2}(\alpha_o r) = \alpha_o\sin(\alpha_o r) - \frac{1}{r}\cosh(\alpha_o r)$. The pressure and the tangential stress are

$$p = \eta\alpha_\circ^2\sum_{n=2}\left(\frac{1}{n-1}\tilde{A}_n r^{n-1} - \frac{1}{n}\tilde{B}_n r^{-n}\right)P_{n-1}(\cos\theta) \tag{52}$$

and

$$\sigma_{r\theta} = 2\eta\sum_{n=2}\left(\begin{array}{c} n(n-2)\tilde{A}_n r^{n-3} + (n^2-1)\tilde{B}_n r^{-n-2} + \dfrac{\tilde{C}_n}{2r^3}\left(n(n-1)y_n(\alpha_\circ r) - 2ry_n{}'(\alpha_\circ r) + r^2 y_n''(\alpha_\circ r)\right) + \\[2mm] + \dfrac{\tilde{D}_n}{2r^3}\left(n(n-1)y_{-n}(\alpha_\circ r) - 2ry_{-n}{}'(\alpha_\circ r) + r^2 y_{-n}''(\alpha_\circ r)\right) \end{array}\right). \tag{53}$$

Stream function for Brinkman equation with variable permeability

For variable permeability $\alpha(r)$, the stream function satisfies the fourth-order differential equation

$$E^4\psi^\star - \alpha^2(r)\left(E^2 + \frac{2}{\alpha(r)}\frac{d\alpha}{dr}\frac{d}{dr}\right)\psi^\star = 0. \tag{54}$$

Upon separation of variables, $\psi^* = R(r)Z(\xi)$, one finds that the differential equation for $Z(\xi)$ and its solution are identical to the case of constant permeability. The differential equation for $R(r)$ is

$$r^4\frac{d^4R}{dr^4} - \left(\alpha^2 r^2 + 2n(n-1)\right)r^2\frac{d^2R}{dr^2}$$
$$- \left(2\alpha r^3\frac{d\alpha}{dr} - 4n(n-1)\right)r\frac{dR}{dr}$$
$$+ n(n-1)\left(\alpha^2 r^2 + n^2 - n - 6\right)R$$
$$= 0. \tag{55}$$

For the special case of $\alpha = \frac{\alpha_\circ}{r}$, the differential equation simplifies to

$$r^4\frac{d^4R}{dr^4} - \left(\alpha_\circ^2 + 2n(n-1)\right)r^2\frac{d^2R}{dr^2} + \left(2\alpha_\circ^2 + 4n(n-1)\right)r\frac{dR}{dr}$$
$$+ n(n-1)\left(\alpha_\circ^2 + n^2 - n - 6\right)R$$
$$= 0. \tag{56}$$

Changing to variable $r = e^\rho$, we get

$$R'''(\rho) - 6R'''(\rho) + \left(-2n(n-1) + 11 - \alpha_\circ^2\right)R''(\rho)$$
$$+ \left(3\alpha_\circ^2 + 6n(n-1) - 6\right)R'(\rho) + n(n-1)$$
$$\left(\alpha_\circ^2 + n^2 - n - 6\right)R(\rho) = 0. \tag{57}$$

The general solution of the above differential equation is of the form $e^{m\rho} = r^m$, where m satisfies the following quartic equation:

$$m^4 - 6m^3 + \left(-2n(n-1) + 11 - \alpha_\circ^2\right)m^2$$
$$+ \left(3\alpha_\circ^2 + 6n(n-1) - 6\right)m + n(n-1)\left(\alpha_\circ^2 + n^2 - n - 6\right)$$
$$= 0.$$

Hence, the stream function is

$$\psi^\star = \sum_{n=2}\left(Ar^{m_1} + Br^{m_2} + Cr^{m_3} + Dr^{m_4}\right)\mathscr{G}_n(\cos\theta), \tag{58}$$

where m_i, $(i = 1, 2, 3, 4)$ are roots of the quartic equation. For $\alpha_o = 0$, we recover the Stokes solutions r^n, r^{-n+1}, r^{n+2}, and r^{-n+3}.

For $n = 2$, the solutions of the quartic equation are

$$m_{1,2,3,4} = \frac{1}{2}\left(3 \pm \sqrt{13 + 2\alpha_\circ^2 \pm 2\sqrt{\left(36 - 4\alpha_\circ^2 + \alpha_\circ^4\right)}}\right). \tag{59}$$

The velocity components are

$$v_r = -\cos\theta\left(Ar^{m_1-2} + Br^{m_2-2} + Cr^{m_3-2} + Dr^{m_4-2}\right). \tag{60a}$$

and

$$v_\theta = \frac{1}{2}\sin\theta\left(m_1 A r^{m_1-2} + m_2 B r^{m_2-2} + m_3 C r^{m_3-2} + m_4 D r^{m_4-2}\right),$$
(60b)

and the pressure and tangential stress components are

$$p = \eta\cos\theta\left[\left(\frac{m_1^2 - m_1 - 2 - \alpha_\circ^2}{m_1 - 3}\right)A\,r^{m_1-3} + \left(\frac{m_2^2 - m_2 - 2 - \alpha_\circ^2}{m_2 - 3}\right)B\,r^{m_2-3} + \left(\frac{m_3^2 - m_3 - 2 - \alpha_\circ^2}{m_3 - 3}\right)C\,r^{m_3-3} + \right.$$
$$\left. +\left(\frac{m_4^2 - m_4 - 2 - \alpha_\circ^2}{m_4 - 3}\right)D\,r^{m_4-3}\right]$$
(61a)

and

$$\sigma_{r\theta} = \eta\sin\theta\left[\left(\frac{3m_1^2 - 11m_1 + 10 - \alpha_\circ^2}{m_1 - 3}\right)A\,r^{m_1-3} + \left(\frac{3m_2^2 - 11m_2 + 10 - \alpha_\circ^2}{m_2 - 3}\right)B\,r^{m_2-3} + \right.$$
$$\left. +\left(\frac{3m_3^2 - 11m_3 + 10 - \alpha_\circ^2}{m_3 - 3}\right)C\,r^{m_3-3} + \left(\frac{3m_4^2 - 11m_4 + 10 - \alpha_\circ^2}{m_4 - 3}\right)D\,r^{m_4-3}\right]$$
(61b)

APPENDIX B: FUNCTIONS $f_1(\chi_1, \chi_2)$ AND $f_2(\chi_1, \chi_2)$:

The functions $f_1(\chi_1, \chi_2)$ and $f_2(\chi_1, \chi_2)$ that appear in Eq. 31 are

$$f_1 = \frac{10}{3}\left(\frac{(\chi_1 - \chi_2)^3\left(4\chi_1^2\chi_2^2 + 7\chi_1\chi_2^3 + 4\chi_2^4\right)}{\Delta_1}\right) \quad \text{and} \quad f_2$$
$$= -\frac{5}{3}\left(\frac{(\chi_1 - \chi_2)\left(\chi_1^4 + \chi_1^3\chi_2 + \chi_1^2\chi_2^2 + \chi_1\chi_2^3 + \chi_2^4\right)\Delta_2}{\Delta_3}\right),$$
(62)

with

APPENDIX C: THE EFFECT OF EXPERIMENTAL NOISE ON THE PREDICTIONS

To study the effect of experimental error on the computed constitutive coefficients, we performed the following numerical experiment:

- First, we assumed an analytical form for the cortex rate of displacements in radial and angular direction. As an example, we considered a sinusoidal form for $\lambda(t)$ and $\lambda'(t)$:

$$\lambda_1(t) = a_\circ + \sum_n a_n\cos(n\omega t) + b_n\sin(n\omega t) \text{ and}$$
$$\lambda\prime_1(t) = a\prime_\circ + \sum_n a\prime_n\cos(n\omega t) + b\prime_n\sin(n\omega t),$$

where a_i, a'_i, b_i, b'_i, and ω were provided as inputs. We consider this to be the "true" rate of displacement, i.e., the results one would obtain from experiments if they had unlimited spatiotemporal resolution.

- Next, we added a white noise of different amplitudes to λ and λ' to model the experimental uncertainties:

$$\Delta_1 = 13\chi_1^5\chi_2^5 + 13\chi_1^4\chi_2^6 + 13\chi_1^3\chi_2^7 + 2\chi_1^5 + 2\chi_1^4\chi_2 + 2\chi_1^3\chi_2^2 + 3\chi_1^2\chi_2^8 + 3\chi_1\chi_2^9 + 12\chi_1^2\chi_2^3 + 12\chi_1\chi_2^4,$$

$$\Delta_2 = 8\left(\chi_2^6 + \chi_2^5 + \chi_2^4 + \chi_2^3 + \chi_2^2\right) - 3\chi_1^4\chi_2^7 - 3\chi_1^4\chi_2^6 + 10\chi_1^4\chi_2^5 + 10\chi_1^4\chi_2^4 + 10\chi_1^4\chi_2^3 - 2\chi_1^4\chi_2^2 - 2\chi_1^4\chi_2 - 3\chi_1^3\chi_2^8$$
$$-3\chi_1^3\chi_2^7 + 10\chi_1^3\chi_2^6 + 10\chi_1^3\chi_2^5 + 10\chi_1^3\chi_2^4 - 2\chi_1^3\chi_2^3 - 2\chi_1^3\chi_2^2 - 21\chi_1^5\chi_2^6 - 21\chi_1^5\chi_2^5 - 8\chi_1^5\chi_2^4 - 8\chi_1^5\chi_2^3$$
$$-8\chi_1^5\chi_2^2 - 2\chi_1^5\chi_2 - 2\chi_1^5 + 3\chi_1^2\chi_2^7 + 3\chi_1^2\chi_2^6 + 3\chi_1^2\chi_2^5 - 10\chi_1^2\chi_2^4 - 10\chi_1^2\chi_2^3 + 2\chi_1^2\chi_2^2 + 2\chi_1^2\chi_2 + 2\chi_1^2 + 3\chi_1\chi_2^8$$
$$+3\chi_1\chi_2^7 + 3\chi_1\chi_2^6 - 10\chi_1\chi_2^5 - 10\chi_1\chi_2^4 + 2\chi_1\chi_2^3 + 2\chi_1\chi_2^2 + 2\chi_1\chi_2,$$

$$\Delta_3 = \left(1 - \chi_1^5\right)\left(\chi_2^4 + \chi_2^3 + \chi_2^2 + \chi_2 + 1\right)\Delta_1.$$
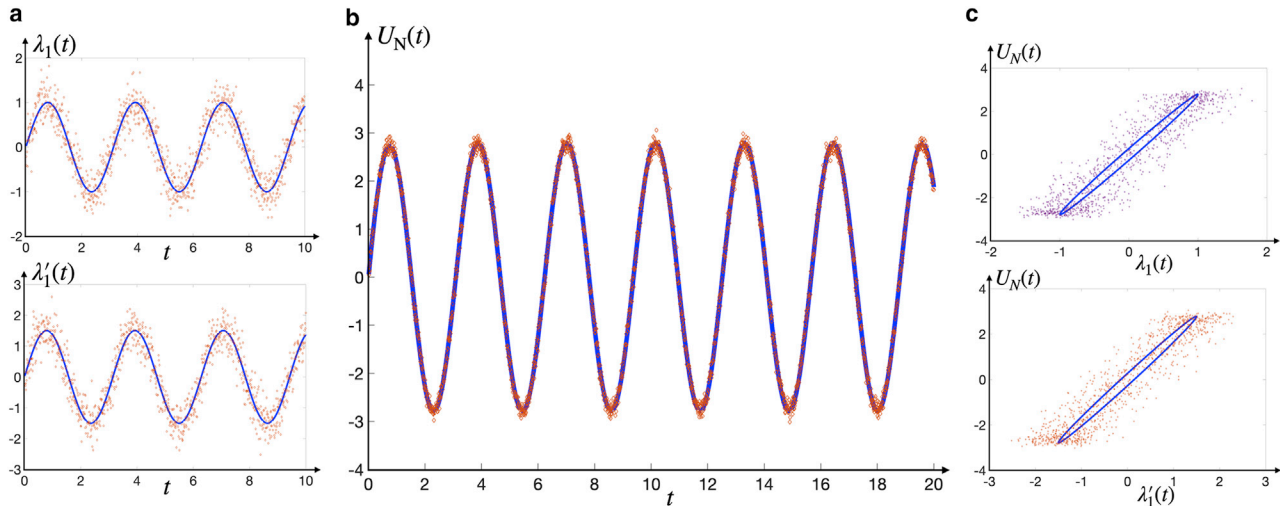
FIGURE 9   (*a*) The radial and tangential time-dependent velocities of the cell cortex with exact forms $\lambda_1(t) = 1.0\sin(\omega t)$ and $\lambda_1'(t) = 1.5\sin(\omega t)$ (*solid lines*), where we choose $\omega = 2$. White noises of amplitudes $A = 0.3$ μm/s and $A' = 0.4$ μm/s are added to model experimental uncertainty, and the results are displayed with dots. (*b*) Velocity of the nucleus, $U_N(t)$, as a function of time induced by these surface velocities (*solid curve*) for a Maxwell fluid with $\tau = 1$, $\eta^* = 2.0$, and geometric variables $\chi_1 = 1/3$ and $\chi_2 = 2/3$. The dots show the results in the presence of white noise with amplitude $A_N = 0.1$ μm/s (*dotted curve*). (*c*) Velocity of the nucleus as a function of λ_1 and λ_1'. To see this figure in color, go online.

$$\lambda_{\exp} = \lambda_1(t) + AW(t) \quad \text{and} \quad \lambda\prime_{\exp} = \lambda\prime_1(t) + A'W(t),$$

where $W(t)$ is the white noise function.

• We then fitted this noisy constructed experimental result to a Fourier expansion up to a suitable frequency; here, we chose to consider up to eight modes:

$$\lambda_{\exp} \approx a_{0,\exp} + \sum_{n=1}^{8} a_{n,\exp}\sin(n\omega_{\exp}t)$$
$$+ b_{n,\exp}\cos(n\omega_{\exp}t), \quad \lambda_{\exp}' \approx a_{0,\exp}'$$
$$+ \sum_{n=1}^{8} a_{n,\exp}'\sin(n\omega_{\exp}t) + b_{n,\exp}'\cos(n\omega_{\exp}t).$$

• The obtained Fourier fit is used as the input to calculate the time-dependent nucleus velocity, $U(t)$, for given values of τ and η^* of the Maxwell viscoelastic model (τ and α_o in the linear poroelastic model).

• To account for experimental error in measuring the nucleus velocity, we added a white noise of a different amplitude to the predicted nucleus velocity, $U(t)$: $U_{\exp}(t) = U(t) + A_N W(t)$.

• Finally, we use nonlinear optimization to find the values of η^* and τ (τ and α_o in the linear poroelastic model) that produce the least total error between the nucleus velocities computed from $\lambda_{\exp}(t)$, $\lambda'(t)$, and the noisy ("experimentally" measured) nucleus velocity $U_{\exp}(t)$.

In the absence of any experimental noise, we expect to recover the exact values of τ and η^* (α_o and τ for the poroelastic case) that were used to construct the "experimental" values of the nucleus velocity, $U_{\exp}(t)$. A significant change

in the computed values of τ and η^* (α_o for the poroelastic case) in the presence of noise in both the measured cortex and the nucleus velocities corresponds to large levels of uncertainty in the measured variables. On the other hand, small variations of the computed values with the noise amplitudes would suggest that the computations are not sensitive to high frequency noise and experimental errors.

For the choices of $\tau = 1$, $\eta^* = 2.0$ ($\alpha_o = 2.3$ for the poroelastic case), and $\lambda_1(t) = 1.0\sin(\omega t)$ and $\lambda_1'(t) = 1.5\sin(\omega t)$ with $\omega = 2$ and the noise levels of $A = 0.3$ μm/s, $A' = 0.4$ μm/s, and $A_N = 0.1$ μm/s, the computed values were $\tau = 0.9085$, $\eta^* = 1.9520$ ($\tau = 0.9370$ and $\alpha_o = 2.4972$ for the poroelastic case); see Fig. 9. These values are within 10% of the correct values, demonstrating the ability of the model to correctly predict the constitutive variables in the presence of experimental noise.

SUPPORTING MATERIAL

AUTHOR CONTRIBUTIONS

M.M. and E.N. designed and performed the research and wrote the manuscript.

ACKNOWLEDGMENTS

REFERENCES

1. Fletcher, D. A., and R. D. Mullins. 2010. Cell mechanics and the cytoskeleton. *Nature.* 463:485–492.

2. Jaalouk, D. E., and J. Lammerding. 2009. Mechanotransduction gone awry. *Nat. Rev. Mol. Cell Biol.* 10:63–73.

3. Dumont, S., and T. J. Mitchison. 2009. Force and length in the mitotic spindle. *Curr. Biol.* 19:R749–R761.

4. Nazockdast, E., and S. Redemann. 2020. Mechanics of the spindle apparatus. *Semin. Cell Dev. Biol.* 107:91–102.

5. Altman, G. H., R. L. Horan, …, D. L. Kaplan. 2002. Cell differentiation by mechanical stress. *FASEB J.* 16:270–272.

6. Howard, J. 2001. Mechanics of Motor Proteins and the Cytoskeleton. Sinauer Associates, Sunderland, MA.

7. Di Carlo, D. 2012. A mechanical biomarker of cell state in medicine. *J. Lab. Autom.* 17:32–42.

8. Darling, E. M., and D. Di Carlo. 2015. High-throughput assessment of cellular mechanical properties. *Annu. Rev. Biomed. Eng.* 17:35–62.

9. Hoffman, B. D., G. Massiera, …, J. C. Crocker. 2006. The consensus mechanics of cultured mammalian cells. *Proc. Natl. Acad. Sci. USA.* 103:10259–10264.

10. Jalai, B., E. Diebold, and B. Buckley. 2016. Parallel flow cytometer using radiofrequency multiplexing. *US Patent App*:15/263,419.

11. Dahl, K. N., S. M. Kahn, …, D. E. Discher. 2004. The nuclear envelope lamina network has elasticity and a compressibility limit suggestive of a molecular shock absorber. *J. Cell Sci.* 117:4779–4786.

12. Yvon, A.-M., P. Wadsworth, and M. A. Jordan. 1999. Taxol suppresses dynamics of individual microtubules in living human tumor cells. *Mol. Biol. Cell.* 10:947–959.

13. Swaminathan, V., K. Mythreye, …, R. Superfine. 2011. Mechanical stiffness grades metastatic potential in patient tumor cells and in cancer cell lines. *Cancer Res.* 71:5075–5080.

14. Krieg, M., G. Fläschner, …, D. J. Müller. 2019. Atomic force microscopy-based mechanobiology. *Nat. Rev. Phys.* 1:41–57.

15. Wirtz, D. 2009. Particle-tracking microrheology of living cells: principles and applications. *Annu. Rev. Biophys.* 38:301–326.

16. Gossett, D. R., H. T. Tse, …, D. Di Carlo. 2012. Hydrodynamic stretching of single cells for large population mechanical phenotyping. *Proc. Natl. Acad. Sci. USA.* 109:7630–7635.

17. Mietke, A., O. Otto, …, E. Fischer-Friedrich. 2015. Extracting cell stiffness from real-time deformability cytometry: theory and experiment. *Biophys. J.* 109:2023–2036.

18. Mokbel, M., D. Mokbel, …, S. Aland. 2017. Numerical simulation of real-time deformability cytometry to extract cell mechanical properties. *ACS Biomater. Sci. Eng.* 3:2962–2973.

19. Fregin, B., F. Czerwinski, …, O. Otto. 2019. High-throughput single-cell rheology in complex samples by dynamic real-time deformability cytometry. *Nat. Commun.* 10:415.

20. Ribeiro, A. S., and K. N. Dahl. 2010. The nucleus as a central structure in defining the mechanical properties of stem cells. *Annu. Int. Conf. IEEE Eng. Med. Biol. Soc.* 2010:831–834.

21. Darling, E. M. 2011. Force scanning: a rapid, high-resolution approach for spatial mechanical property mapping. *Nanotechnology.* 22:175707.

22. Mofrad, M. R., and R. D. Kamm. 2006. Cytoskeletal Mechanics: Models and Measurements in Cell Mechanics. Cambridge University Press, Cambridge, UK.

23. Fabry, B., G. N. Maksym, …, J. J. Fredberg. 2001. Scaling the microrheology of living cells. *Phys. Rev. Lett.* 87:148102.

24. Pullarkat, P. A., P. A. Fernández, and A. Ott. 2007. Rheological properties of the eukaryotic cell cytoskeleton. *Phys. Rep.* 449:29–53.

25. Janmey, P. A., and C. A. McCulloch. 2007. Cell mechanics: integrating cell responses to mechanical stimuli. *Annu. Rev. Biomed. Eng.* 9:1–34.

26. Trepat, X., G. Lenormand, and J. J. Fredberg. 2008. Universality in cell mechanics. *Soft Matter.* 4:1750–1759.

27. Mahaffy, R. E., S. Park, …, C. K. Shih. 2004. Quantitative analysis of the viscoelastic properties of thin regions of fibroblasts using atomic force microscopy. *Biophys. J.* 86:1777–1793.

28. Cai, P., Y. Mizutani, …, T. Okajima. 2013. Quantifying cell-to-cell variation in power-law rheology. *Biophys. J.* 105:1093–1102.

29. Cartagena, A., and A. Raman. 2014. Local viscoelastic properties of live cells investigated using dynamic and quasi-static atomic force microscopy methods. *Biophys. J.* 106:1033–1043.

30. Lim, C. T., E. H. Zhou, and S. T. Quek. 2006. Mechanical models for living cells–a review. *J. Biomech.* 39:195–216.

31. Yeung, A., and E. Evans. 1989. Cortical shell-liquid core model for passive flow of liquid-like spherical cells into micropipets. *Biophys. J.* 56:139–149.

32. Strychalski, W., and R. D. Guy. 2016. Intracellular pressure dynamics in blebbing cells. *Biophys. J.* 110:1168–1179.

33. Alt, W., and M. Dembo. 1999. Cytoplasm dynamics and cell motion: two-phase flow models. *Math. Biosci.* 156:207–228.

34. Gracheva, M. E., and H. G. Othmer. 2004. A continuum model of motility in ameboid cells. *Bull. Math. Biol.* 66:167–193.

35. Moeendarbary, E., L. Valon, …, G. T. Charras. 2013. The cytoplasm of living cells behaves as a poroelastic material. *Nat. Mater.* 12:253–261.

36. Diebold, E. D., B. W. Buckley, …, B. Jalali. 2013. Digitally synthesized beat frequency multiplexing for sub-millisecond fluorescence microscopy. *Nat. Photonics.* 7:806–810.

37. Mikami, H., J. Harmon, …, K. Goda. 2018. Ultrafast confocal fluorescence microscopy beyond the fluorescence lifetime limit. *Optica.* 5:117–126.

38. Rosendahl, P., K. Plak, …, J. Guck. 2018. Real-time fluorescence and deformability cytometry. *Nat. Methods.* 15:355–358.

39. Liu, J., G. H. Koenderink, …, D. A. Weitz. 2007. Visualizing the strain field in semiflexible polymer networks: strain fluctuations and nonlinear rheology of F-actin gels. *Phys. Rev. Lett.* 98:198304.

40. Tharmann, R., M. M. Claessens, and A. R. Bausch. 2007. Viscoelasticity of isotropically cross-linked actin networks. *Phys. Rev. Lett.* 98:088103.

41. Vos, B. E., L. C. Liebrand, …, G. H. Koenderink. 2017. Programming the mechanics of cohesive fiber networks by compression. *Soft Matter.* 13:8886–8893.

42. Ricketts, S. N., M. L. Francis, …, R. M. Robertson-Anderson. 2019. Varying crosslinking motifs drive the mesoscale mechanics of actin-microtubule composites. *Sci. Rep.* 9:12831.

43. Muñoz, H. E., M. Li, …, D. Di Carlo. 2018. Single-cell analysis of morphological and metabolic heterogeneity in Euglena gracilis by fluorescence-imaging flow cytometry. *Anal. Chem.* 90:11280–11289.

44. Hoffman, B. D., and J. C. Crocker. 2009. Cell mechanics: dissecting the physical responses of cells to force. *Annu. Rev. Biomed. Eng.* 11:259–288.

45. Sollich, P. 1998. Rheological constitutive equation for a model of soft glassy materials. *Phys. Rev. E.* 58:738–759.

46. Mandadapu, K. K., S. Govindjee, and M. R. Mofrad. 2008. On the cytoskeleton and soft glassy rheology. *J. Biomech.* 41:1467–1478.

47. Djordjević, V. D., J. Jarić, …, D. Stamenović. 2003. Fractional derivatives embody essential features of cell rheological behavior. *Ann. Biomed. Eng.* 31:692–699.

48. Bonfanti, A., J. Fouchard, …, A. Kabla. 2020. A unified rheological model for cells and cellularised materials. *R. Soc. Open Sci.* 7:190920.

49. Hyun, K., M. Wilhelm, …, G. H. McKinley. 2011. A review of nonlinear oscillatory shear tests: analysis and application of large amplitude oscillatory shear (LAOS). *Prog. Polym. Sci.* 36:1697–1753.

50. Sangani, A. S., and A. Acrivos. 1982. Slow flow past periodic arrays of cylinders with application to heat transfer. *Int. J. Multiph. Flow.* 8:193–206.

51. Nazockdast, E., A. Rahimian, …, M. Shelley. 2017. Cytoplasmic flows as signatures for the mechanics of mitotic positioning. *Mol. Biol. Cell.* 28:3261–3270.

52. Isermann, P., and J. Lammerding. 2013. Nuclear mechanics and mechanotransduction in health and disease. *Curr. Biol.* 23:R1113–R1121.

53. Schreiber, K. H., and B. K. Kennedy. 2013. When lamins go bad: nuclear structure and disease. *Cell.* 152:1365–1375.

54. Wolf, K., M. Te Lindert, …, P. Friedl. 2013. Physical limits of cell migration: control by ECM space and nuclear deformation and tuning by proteolysis and traction force. *J. Cell Biol.* 201:1069–1084.

55. Happel, J., and H. Brenner. 2012. Low Reynolds Number Hydrodynamics: With Special Applications to Particulate MediaVolume 1. Springer Science & Business Media, the Netherlands.